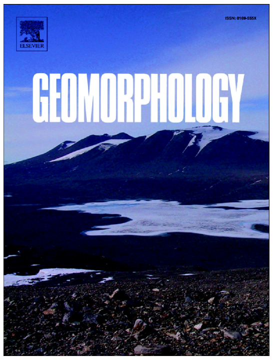

Unravelling the geological and geomorphological evolution of the Terra Cimmeria-Nepenthes Mensae transitional zone, Mars

Ángel García-Arnay, Francisco Gutiérrez

PII: S0169-555X(23)00061-2
DOI: https://doi.org/10.1016/j.geomorph.2023.108641
Reference: GEOMOR 108641

To appear in: *Geomorphology*

Received date: 5 September 2022
Revised date: 26 February 2023
Accepted date: 27 February 2023

Please cite this article as: Á. García-Arnay and F. Gutiérrez, Unravelling the geological and geomorphological evolution of the Terra Cimmeria-Nepenthes Mensae transitional zone, Mars, *Geomorphology* (2023), https://doi.org/10.1016/j.geomorph.2023.108641

Unravelling the geological and geomorphological evolution of the Terra Cimmeria-Nepenthes Mensae transitional zone, Mars

Ángel García-Arnay[(a)*], Francisco Gutiérrez[(a)]

[a] Departamento de Ciencias de la Tierra, Universidad de Zaragoza, 50009 Zaragoza, Spain

* Corresponding author e-mail address: arnay@unizar.es

Abstract

The Terra Cimmeria-Nepenthes Mensae Transitional Zone comprises two highly contrasting geologic-geomorphic domains bounded by the dichotomy escarpment in the equatorial region of Mars. This research provides insight into the geological and geomorphological evolution of the poorly explored NW Terra Cimmeria and SE Nepenthes Mensae. A detailed study largely based on cartographic work and complemented by multiple analyses focused on crater densities, spectral data and radar profiles reveals that (1) the exposed geological record of this transitional zone formed over a long time-span from the Early Noachian to recent times, (2) the inferred compressional and extensional tectonic stresses shaped the landscape at least from the Late Noachian to Late Hesperian, and (3) extensional tectonics, which post-dated the compressional deformation, has controlled the development and evolution of the 2-km-high dichotomy escarpment, the system of NW-SE-oriented basins that used to host paleolakes from the Late Noachian to Late Hesperian, and the fissure volcanism in their deepest areas. These findings shed light into the fundamental morphogenetic role played by compressional and extensional tectonics, and fluvio-lacustrine activity on the configuration of the landscape in these regions. This work provides a reference geologic-geomorphologic framework for future studies in this area and other sectors along the highland-lowland transitional zone of Mars.

Keywords: Mars; Planetary mapping; Dichotomy boundary; Tectonic geomorphology

1. Introduction

The highland-lowland transition, often referred to as the crustal dichotomy (McCauley et al., 1972), represents one of the most prominent geomorphic features on the surface of Mars (Solomon et al., 2005), formed during the early Noachian (Tanaka et al., 1992a). This hemispheric feature that circumscribes the planet bounds two contrasting geologic and geomorphic domains comprised by the ancient, densely cratered and rough highland plateaus in the south, and the younger, sparsely cratered and relatively smooth lowland plains in the north (Morgan et al., 2009). The geomorphic expression of the Martian dichotomy varies laterally, ranging from an escarpment up to 3 km in local relief (Irwin et al., 2004), like the one with associated residual reliefs of highland materials in Nilosyrtis Mensae (Levy et al., 2007), to gently sloping surfaces with no obvious scarp as occurs in northern Arabia Terra (McGill, 2000). The highland-lowland boundary cannot be traced along the Tharsis region, where its geomorphic expression has probably been obliterated by more recent volcanic materials (Zuber et al., 2000).

Studies carried out along the upland-lowland boundary have put forward various endogenic and exogenic interpretations for its formation (McGill and Squyres, 1991), which remains as an unresolved problem (e.g., Andrews-Hanna et al., 2008; Golabek et al., 2011). The main externally-driven hypotheses include: (1) a single "mega-impact" event responsible for the creation of the "Borealis basin" (Wilhelms and Squyres, 1984), (2) the impact "megadome" hypothesis, according to which the melt generated by a giant impact overfilled the impact basin to form the highlands (Reese et al., 2011), and (3) multiple impact depressions merged into a large basin forming the lowlands in the northern hemisphere (Frey et al., 1986; Frey and Shultz, 1988). Several endogenic hypotheses have also been proposed: (1) long-wavelength mantle convection resulting in large-scale upwelling (Zhong and Zuber, 2001; Roberts and Zhong, 2006; Ke and Solomatov, 2006), (2) long-wavelength "cumulate overturn" of a stratified magma ocean resulting from the crystallization of an early magma ocean (Elkins- Tanton et al., 2005), and (3) an early plate tectonics phase involving the creation of a thin crust in the northern hemisphere from relict spreading centers, with the crustal dichotomy representing a passive margin (Sleep, 1994). The models based on multiple impacts and plate tectonics to explain the origin of the dichotomy have not been sufficiently supported and remain as untested hypotheses (Roberts, 2015). Although the origin of the dichotomy remains as an open issue, it seems probable that multiple processes may have operated in conjunction to form this major geomorphic feature (Reese et al., 2010), which may have been subsequently modified by tectonic, fluvial, glacial, eolian, and mass wasting processes (Watters and Robinson, 1999; Tanaka et al., 2005).

The geomorphic expression of the highland-lowland boundary in Aeolis Mensae (e.g., Irwin et al., 2004; Irwin et al., 2005) is like that found between the cratered highlands of the northwest part of Terra Cimmeria and the lowland plains of the southeast zone of Nepenthes Mensae analyzed in this work. Both regions are characterized by the occurrence of a remarkable dichotomy escarpment (~2 km in local relief) and closed depressions in the lowlands interrupted by mesas and knobs (relatively small, rounded hills) made up of materials of the highland plateau (see Fig. 1a, b). According to Irwin et al. (2004), the latter landforms probably correspond to residual outcrops resulting from fracture-controlled differential erosion acting along the edge of the escarpment. In these regions, as well as in Nilosyrtis Mensae, the highland residuals north of the escarpment show an increasing degree of degradation grading northward from mesas to sparse knobs (Irwin et al., 2004). The approximate alignment of mesa margins, buttes and knobs in Nilosyrtis Mensae, as well as the straightness and orientation of valleys, mostly parallel to the dichotomy escarpment, have been associated with the occurrence of Noachian-aged grabens along the crustal dichotomy (Levy et al., 2007). These transitional provinces show various morpho-tectonic features such as fracture-controlled linear valleys known as fretted valleys, extensional troughs forming chains of closed depressions in the lowlands, and lobate scarps ascribable to thrust faults in the adjacent highlands (McGill and Dimitriou, 1990; Watters, 2003a, 2003b; Watters and McGovern, 2006).

This work is focused on the highly contrasting transitional zone of NW Terra Cimmeria and SE Nepenthes Mensae (Fig. 1a, b), which remains as a poorly understood area (e.g., Skinner and Tanaka, 2018) and offers the opportunity for gaining insight into the processes involved in the development and evolution of the dichotomy escarpment. This area has been covered by multiple global and regional geologic maps produced by the United States Geological Survey (USGS) (e.g., King, 1978; Scott and Carr, 1978; Hiller, 1979; Greeley and Guest, 1987; Tanaka et al., 1992b; Tanaka et al., 2005; Tanaka et al., 2014). Recently, Skinner and Tanaka (2018) produced a regional-scale geologic map of the transition zone between Terra Cimmeria and Utopia Planitia, which is located northwest of our study area. Due to its proximity, this map provides a geological framework with which to compare our study. In the last few years, several authors have highlighted the important role played by surface water on the configuration of NW Terra Cimmeria and SE Nepenthes Mensae (e.g., Goudge and Fassett, 2018; Rivera-Hernández and Palucis, 2019; García-Arnay and Gutiérrez, 2020). Specifically, putative deltas, shore platforms and paleolakes associated with a belt of closed depressions distributed along the foot of the dichotomy escarpment illustrate the value of geomorphic studies for understanding the role of the hydrosphere of Mars in the past (García-Arnay and Gutiérrez, 2020). However, despite its importance, there is a lack of detailed cartographic studies to furnish knowledge about the geological context and the evolution of this transitional zone. Areas located close to our study region have been selected as landing sites for several missions due to their low latitude, potential for paleoenvironmental research, and/or pervasive planarity (e.g., NASA's Mars Science Laboratory "Curiosity" and InSight missions settled in Gale crater and SW Elysium Planitia, respectively). The Nepenthes Planum region has been also targeted as a favorable landing site over time (e.g., NASA's Viking lander 1, Mars Pathfinder and Mars Exploration Rover missions or ESA's Beagle 2 mission), but finally discarded due to lack of sufficient knowledge about its geology (Skinner and Tanaka, 2018).

In this study, we have carried out a comprehensive local- and regional-scale geological study of NW Terra Cimmeria and SE Nepenthes Mensae largely based on cartographic work with the following purposes: (1) improve our knowledge on the geology and geomorphology of this transitional zone; (2) infer the processes responsible for the formation of the system of closed depressions that used to host paleolakes; (3) analyze the evolution of the dichotomy escarpment; and (4) reconstruct the geological-geomorphological history of the region. To achieve these objectives, we have produced a detailed geologic-geomorphic map identifying and describing the different units and features, analyzing their geometrical relationships, and correlating the units with those of the previous geological maps. We have also inferred the mineral composition of surface materials of paleoenvironmental interest, estimated the age of the main mapped units, and interpreted subsurface structures from the analysis of radargrams.

2. Regional setting in the highland-lowland boundary

The study area is in the Terra Cimmeria-Nepenthes Mensae Transitional Zone (CNTZ), comprising two contrasting geologic-geomorphic domains bounded by the dichotomy escarpment, in the equatorial region of Mars (Fig. 1a). The sector of the CNTZ analyzed in this work corresponds to the northwest part of Terra Cimmeria and the southeast zone of Nepenthes Mensae. Terra Cimmeria forms part of the highland province, south of the dichotomy boundary, and was mapped as a Middle Noachian highland unit (mNh) characterized by moderately to heavily degraded terrains formed by undifferentiated impact, volcanic, fluvial and basin materials, according to the most recent global geological map of Mars (Tanaka et al., 2014). This heavily cratered region has been tectonically contracted, as indicated by the presence of numerous lobate scarps and wrinkle ridges (e.g., Watters and Robinson, 1999). It is also dissected by ancient V-shaped fluvial valleys (e.g., Irwin and Howard, 2002), with mouths located along the dichotomy escarpment, with a local relief of around 2 km. The valleys seem to be locally disrupted by compressional tectonic deformation, suggested by the occurrence of beheaded channels associated with lobate scarps. They also show a clear structural control in the vicinity of the dichotomy, following the orientation of morpho-structural troughs both subparallel and subperpendicular to the escarpment, probably generated by extensional tectonic deformation and/or lateral spreading along the dichotomy (see Fig. 2a). Licus Vallis, which is the main ancient fluvial valley in the study area, shows an apparently poorly evolved watershed, as suggested by its convex hypsometric curve and a very low drainage density (García-Arnay et al., 2018b). The paired terraces and knickpoints observed within this and other valleys seem to support base-level variations in the mouth area of the watersheds and/or rejuvenation by vertical tectonic movements (Goudge and Fassett, 2018). Furthermore, the majority of the valley networks, including Licus Vallis, show moderately preserved fan-shaped deposits at their mouths, most of them interpreted as putative Gilbert-type deltas and alluvial fans (e.g., Irwin et al., 2005; de Pablo and Pacifici, 2008; García-Arnay et al., 2018a, b; Rivera-Hernández and Palucis, 2019; García-Arnay and Gutiérrez, 2020).

The terrains north of Terra Cimmeria correspond to the region of Nepenthes Mensae, which is part of the transitional province north of the dichotomy. It was mapped as a Hesperian and Noachian transition unit (HNt) and described as Noachian impact breccias, volcanic rocks, and aprons formed by mass-wasted deposits during the Hesperian (Tanaka et al., 2014). This region displays two contrasting areas: (1) tectonically-contracted plateaus with eolian erosional landforms, and (2) a belt of interconnected NW-SE-trending closed depressions at the foot of the dichotomy escarpment in the knobby terrain (Irwin et al., 2004). These closed depressions together with the dichotomy escarpment are probably related to extensional deformation (Watters, 2003a; Watters and McGovern, 2006) (see Fig. 1b). Both areas display numerous residual outcrops (mesas and knobs) formed by highland materials. The presence of structural elements along the dichotomy may have also controlled the erosion pattern of the highlands, as suggested by fracture-controlled erosional troughs displayed by residual reliefs such as mesas (see Fig. 2a). The identification of fan-shaped deposits and coastal-like benches associated with the closed depressions, interpreted as putative Gilbert-type deltas and paleoshore platforms, respectively (García-Arnay and Gutiérrez, 2020), may be attributable to landforms developed along the shores of interconnected paleolakes.

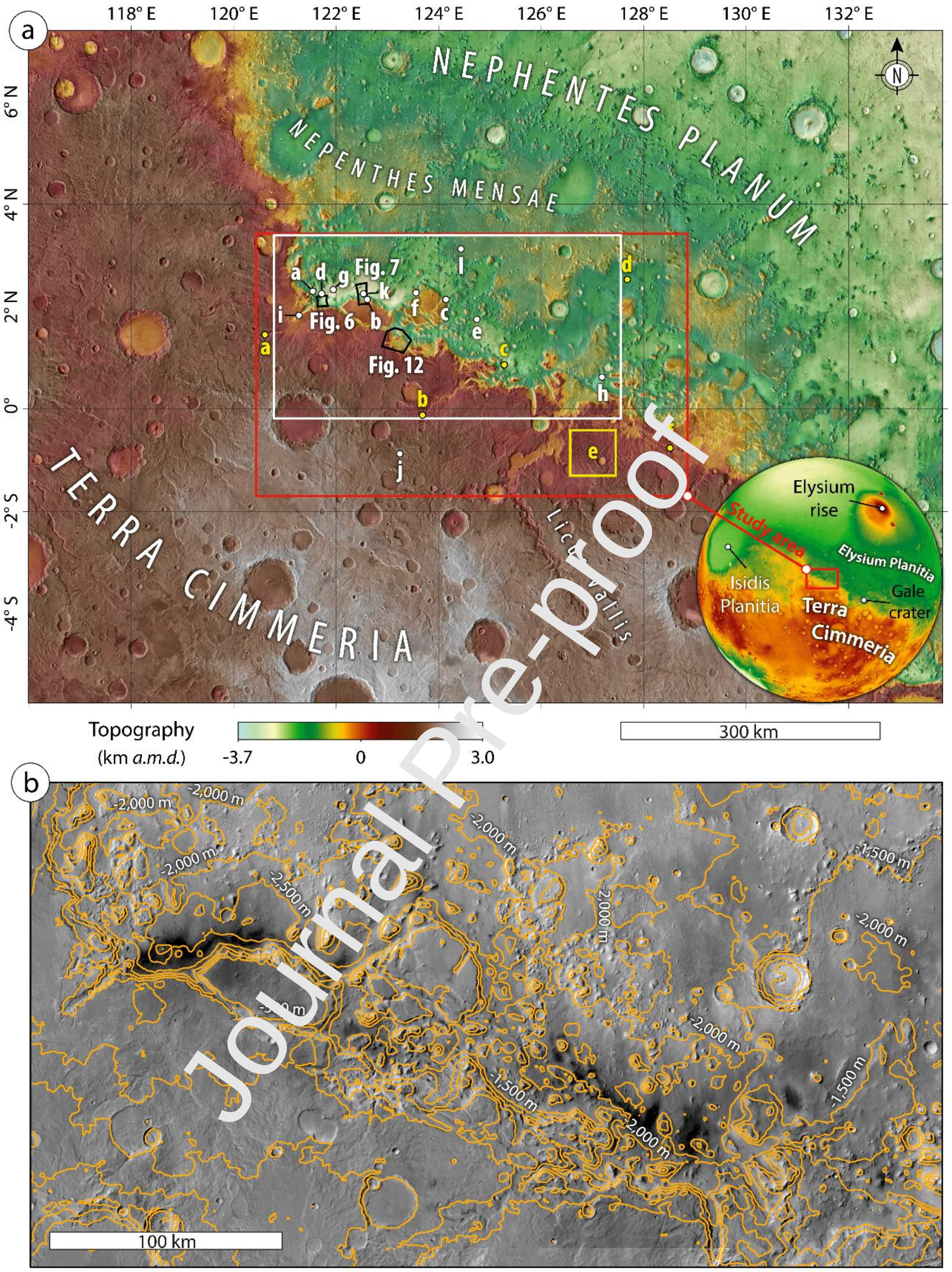

Fig. 1. (a) Colorized elevation model (km above Martian datum) derived from HRSC-MOLA blended data over a base mosaic map of THEMIS-IR day images, with the study area framed by the red rectangle. The small white circles and the small yellow circles/boxes, as well as their corresponding labels indicate the position of the images

shown in Figs. 3 and 4, respectively. The white polygon indicates the location of the CTX image shown in (b). Black polygons indicate the area covered by the 3D model of Fig. 12, and the location of the CRISM images shown in Figs. 6 and 7 (b) Interconnected closed depressions in the Nepenthes Mensae region showing 500-m contour intervals. Darker areas at the foot of the dichotomy escarpment are associated with dark-toned dunes (CTX image mosaic).

3. Data and methods

Images, topographic and spectral data, as well as radar profiles were used to map and infer the geology, geomorphology, age, surface composition, and internal structure of the CNTZ. Visible images included panchromatic images acquired by the Context Camera (CTX, 5-6 m/pixel) (Malin et al., 2007), and additional images from the High Resolution Imaging Science Experiment (HiRISE, ~25-50 cm/pixel) (McEwen et al., 2007), both instruments on board NASA's Mars Reconnaissance Orbiter. The global CTX image mosaic (Dickson et al., 2018) covers the totality of the CNTZ, whereas HiRISE images cover specific zones of the study area. Infrared images comprised the daytime infrared image mosaic obtained by the Thermal Emission Imaging System (THEMIS, 100 m/pixel) (Edwards et al., 2011; Christensen et al., 2004, 2013), on board NASA's Mars Odyssey. In order to differentiate surface materials on the basis of their thermophysical properties, we used the THEMIS-based thermal inertia (TI) (Fergason et al., 2006), which is derived from the nighttime infrared image mosaic captured by THEMIS.

Topographic data were extracted from Digital Elevation Models (DEMs) acquired by instruments with different spatial resolutions and coverages: laser altimeter point shotconstrained global gridded data from the Mars Orbiter Laser Altimeter (MOLA, 463 m/pixel) (Zuber et al, 1992), on board NASA's Mars Global Surveyor, as well as stereo-pair images from the High Resolution Stereo Camera (HRSC, 50-75 m/pixel), on board ESA's Mars Express. The characterization and morphometric analysis of the landforms were carried out using, where possible, the HRSC-derived topographic data that displays the best spatial resolution. In order to cover areas where HRSC data are not available, we used a HRSC and MOLA blended DEM (Fergason et al., 2018, ~200 m/pixel). The images and topographic data were integrated into a Geographic Information System (ESRI's ArcGIS 10.5.1) to map and carry out multiple analyses. Spatial data were projected into the geographic coordinate system "GCS_Mars_2000_Sphere", with an equidistant cylindrical projection and a central meridian of 125ºE, which is approximately located in the center of the CNTZ.

The geologic-geomorphic map (Fig. 2a) was produced applying standard methodologies and techniques used in planetary geological mapping (e.g., Greeley and Batson, 1990; Wilhelms, 1990), as well as in geological mapping of Mars (e.g., Skinner and Tanaka, 2003; Tanaka et al., 2014; Skinner and Tanaka, 2018). We mainly used a combination of images (visible and infrared) and topographic data that permitted the identification of the surface units based on their primary surface features (Skinner and Tanaka, 2003). This approach was also used for the characterization of the units, the analysis of their geometrical relationships, and their correlation. The mapping scale varies across the study area according to the resolution of the spatial data, ranging between ~0.25 and 100 m (minimum size of identifiable features). We used the THEMIS daytime infrared image mosaic as a primary base map to identify the lateral extent of the units. CTX and HiRISE images, as well as the TI mosaic, were used as supplementary datasets for refining the mapping of the boundaries of the units and interpreting their origin. The spectral data provided information on the mineral composition of some units of special interest (e.g., putative delta deposits and volcanic materials). The mapped units were named (see Fig. 2a) based on their geographic location, where applicable, dominant landforms and/or genesis, as well as stratigraphic relations, in order to maintain consistency (Hansen, 2000; Tanaka et al., 2005; Skinner and Tanaka, 2018). The units were also labeled and grouped (Fig. 2a) following an analogous methodology to that applied by Skinner and Tanaka (2018) for the geological map of Nepenthes Planum. The drainage network was initially mapped automatically using the "Hydrology" toolset in ArcGIS and was later improved by manually removing numerous artifacts using visible images and TI data. The frequent occurrence of unconsolidated sediments (e.g., eolian deposits) in the valley floors, characterized by a lower apparent TI (Fig 2c), helped to improve the delineation of the drainage network. The mapping of the putative deltas and alluvial fans was challenging due to their moderate preservation conditions. Some of the fan-shaped deposits in the study area lack clear proximal edges (i.e., upstream). To address this, we decided to delineate the proximal edges of the putative deltas and alluvial fans where the ancient flows debouching from the fluvial valleys in this study became unconfined, which resulted in the deposition of the fan-shaped accumulation. We proposed this approach in García-Arnay and Gutiérrez (2020) related to the analysis of the putative deltas in Nepenthes Mensae.

Based on the new map, we present an updated summary table of both new and previously published putative deltas and alluvial fans located within and in the vicinity of the study area (see Table 1, and Figs. 3e-g and 4f). Elevation values were extracted from the slope break between the delta plain and the delta front junction, interpreted as the mean highstand level (e.g., Di Achille and Hynek, 2010). Several morphological features were also described such as layering, the occurrence of lobes and stepped profiles, or the type of watershed. All crater rims >5 km in diameter have been mapped. Well-preserved and pervasive crater materials with rim diameter ranging between 5 and 13 km were mapped as “Crater unit – undivided”. This unit does not distinguish the different crater-related components due to their relatively small size in comparison with the map scale. In contrast, the preserved components (i.e., rim, wall, floor, peak, and ejecta) of craters ≥13 km in rim diameter were depicted in the map. Azimuth data from mapped landforms of interest (troughs and volcanic ridges) were extracted automatically with the “Minimum Bounding Geometry” tool available on “Data Management” toolbox of ArcGIS and plotted on rose diagrams with GeoRose 0.5.1 software (Yong Technology Inc.) (see Fig. 5).

Spectral analysis allows us to infer the mineral composition of the surface, which in turn strengthens our interpretation on the origin and formation processes of the analyzed surface units. The mineral composition of the surficial material of units of interest was inferred from hyperspectral data obtained by the Compact Reconnaissance Imaging Spectrometer for Mars (CRISM, ~18-36 m/pixel) (Murchie et al., 2007), onboard NASA’s Mars Reconnaissance Orbiter. The CRISM instrument is a visible to near-infrared imaging spectrometer with a wavelength range from 0.362 to 3.92 µm. We selected CRISM data with corrected I/F (radiance/solar irradiance) from the Targeted Empirical Record (TER) and the Map-projected Targeted Reduced Data Record (MTRDR). The spectral analysis was carried out using the CRISM Analysis Toolkit (CAT, version 7.3.1), an IDL/ENVI-based software system developed by the CRISM Science Team (Morgan et al., 2014). Spectral curves and spectral parameter maps were obtained, respectively, from the corrected I/F, and the refined spectral summary parameters (Viviano-Beck et al., 2014). We analyzed two CRISM scenes:

FRT00017610 (~18 m/pixel, ~10x10 km) and HRL000134F5 (~36 m/pixel, ~10x20 km) to determine the composition of surface material in two different areas with paleoenvironmental interest. These CRISM scenes include fan-shaped deposits previously interpreted as putative deltas, and spatially associated fluvial and volcanic deposits (Figs. 6a and 7a). The occurrence of clay-bearing surfaces was identified on spectral parameter maps obtained by the PHY product (D2300 -red-, D2200 -green-, BD1900r2 -blue-) for both projected CRISM scenes following the procedure described by Viviano-Beck et al. (2014) (see Figs. 6b and 7c). Surfaces with olivine-bearing deposits were detected from the spectral parameter map derived from the MAF product (OLINDEX3 -red-, LCPINDEX2 -green-, HCPINDEX2 -blue-) for the projected CRISM scene HRL000134F5 (see Fig. 7b). The detection of clay- and olivine-rich surfaces suggests, respectively, the past existence of water and volcanic activity in the region. To highlight these compositional units (i.e., clay- and olivine-bearing units), we adjusted the values displayed for each RGB channel applying stretch limits. I/F spectra were extracted from the unprojected CRISM scene FRT00017610 and averaged from a Region of Interest (ROI) selected for each compositional unit to obtain average spectra (s1). In order to minimize atmospheric and dust contributions and instrument artifacts, these average spectra (s1) were ratioed to an average spectrum from a ROI of relatively spectrally featureless materials (s2) extracted from the CRISM scene. The ratioed I/F spectra (s1/s2) were compared with the CRISM and ENVI spectral libraries (Viviano-Beck et al., 2015) (Figs. 6c, d) to identify minerals that best match to CRISM spectra.

Age dating of surface units was carried out following the procedure proposed by Warner et al. (2015). Crater-counting areas for each unit of interest (Fig. 2b) and their associated crater populations were mapped and computed using the “CraterTools” toolset for ESRI’s ArcGIS (Kneissl et al., 2011). Depending on the spatial resolution and noise level of the visible images available (i.e., CTX or HRISE), all primary craters larger than 50 or 100 m in diameter (threshold values) with geometric centers within the count area were mapped manually based on three points selected along the crater rim. In general, we decided to exclude from our count areas the surfaces occupied by well-preserved ejecta blankets and their superposed crater populations because they represent the age of the impact event and postdate the target surface (Warner et al., 2015). However, crater populations on ejecta blankets were included when it was necessary to estimate the age of the associated impact event. To minimize any potential bias derived from the variable cratering pattern, we selected, where possible, crater-counting areas larger than 1,000 km^2 (Warner et al., 2015). Crater size-frequency diagrams for each sampling area (Fig. 8) were generated using CraterStats2 software (Michael and Neukum, 2010) and absolute model ages were derived from crater production and chronology functions defined by Hartmann (2005). The age of the units (i.e., the age range estimated for the end of their formation), as well as the final age of the resurfacing events were estimated from simple and corrected cumulative data-dependent fits, respectively (see summarized age chart in Fig. 10). Assignment of the chronologic period(s) and epoch of Mars (Michael, 2013) to each mapped unit, which is indicated in the unit codes in capital letters (see map legend in Fig. 2a), was based on both the age estimates obtained by crater counting and their relative chronology inferred from geometrical relationships.

The analysis of radargrams contributed to the interpretation of the subsurface structure of the CNTZ (see Fig. 9). We selected 8 radargrams located across the CNTZ (from West to East: S_01966502, S_02617902, S_01832001, S_02674602, S_02596802, S_01981001, S_01846503, S_02569101) that were obtained by the Mars Shallow Radar Sounder (SHARAD) (Seu et al., 2007), on board NASA’s Mars

Reconnaissance Orbiter. These NE-SW-oriented radargrams were analyzed with the JMARS 5 software (ASU's Mars Space Flight Facility), which permitted us in combination with geomorphic data to identify possible tectonic and stratigraphic features. A surface clutter analysis was carried out to distinguish subsurface reflections on radargrams from cross-track surface echoes, also known as “surface clutters” (e.g., Choudhary et al., 2016). This analysis consisted of the comparison of the radargram with its associated simulated cluttergram. The identification of reflections on the radargram and its related cluttergram suggests that such echoes are due to surface reflections rather than subsurface returns. Geologic cross-sections shown in Figs. 11 and 13 summarize our interpretation of the subsurface stratigraphic relationships among the units, as well as the possible tectonic structures that occur along the profiles. They were constructed based on the information provided by radargrams, topographic data, the geologic units, as well as the spectral analysis and formation ages of the units.

4. Results

4.1 Geology and geomorphology of the CNTZ

We have produced a detailed geological-geomorphological map of the CNTZ in order to identify and characterize the geologic units and the geomorphic features, establishing their spatial relationships and relative chronology (Fig. 2a). In our map we have recognized 18 units, which have been grouped according to their geographic distribution as follows: three units in the Cimmeria region of the highland province, two units in the Nepenthes Mensae region of the highland-lowland transitional province, seven impact crater units, and six spatially dispersed units. Furthermore, we have depicted the main geomorphic features that occur within the units.

4.1.1 Description of the units

The Cimmeria region units include two Cimmeria dissected units (Nhcd$_a$ and Nhcd$_b$) and the Cimmeria basin unit (Nhc$_b$) (Fig. 2a). Both Cimmeria dissected units are characterized by rugged and heavily cratered surfaces dissected by V-shaped valley networks (e.g., Tanaka et al., 2005, 2014; Skinner and Tanaka, 2018). These units represent two well-differentiated members. Member 'a' (Nhcd$_a$) crops out in the topographically higher portion of the highland province, mainly in the southwest sector of the mapped area. It displays a higher crater density than member 'b', lobate scarps with a dominant NW-SE orientation subparallel to the dichotomy, and less frequently ridge crests. Member 'b' of the Cimmeria dissected unit (Nhcd$_b$) occurs in the plateau situated south of the dichotomy escarpment at lower elevation than member 'a' (Nhcd$_a$), and is represented by residual reliefs (e.g., mesas and knobs) in the transitional province. This heavily dissected but less-cratered member exhibits deeper valleys with a dominant NE-SW orientation and a secondary NW-SE trend, the latter of which seem to be related to the numerous fracture-controlled troughs that occur in the vicinity of the dichotomy escarpment (see Figs. 2a and 5a). Member b locally exhibits NE-SW-oriented ridge crests in the eastern sector of the unit, and scarce occurrence of lobate scarps with NW-SE orientation. The boundary between members 'a' and 'b' is gradational, mainly defined by the slope break between the higher southern reliefs and the plateau.

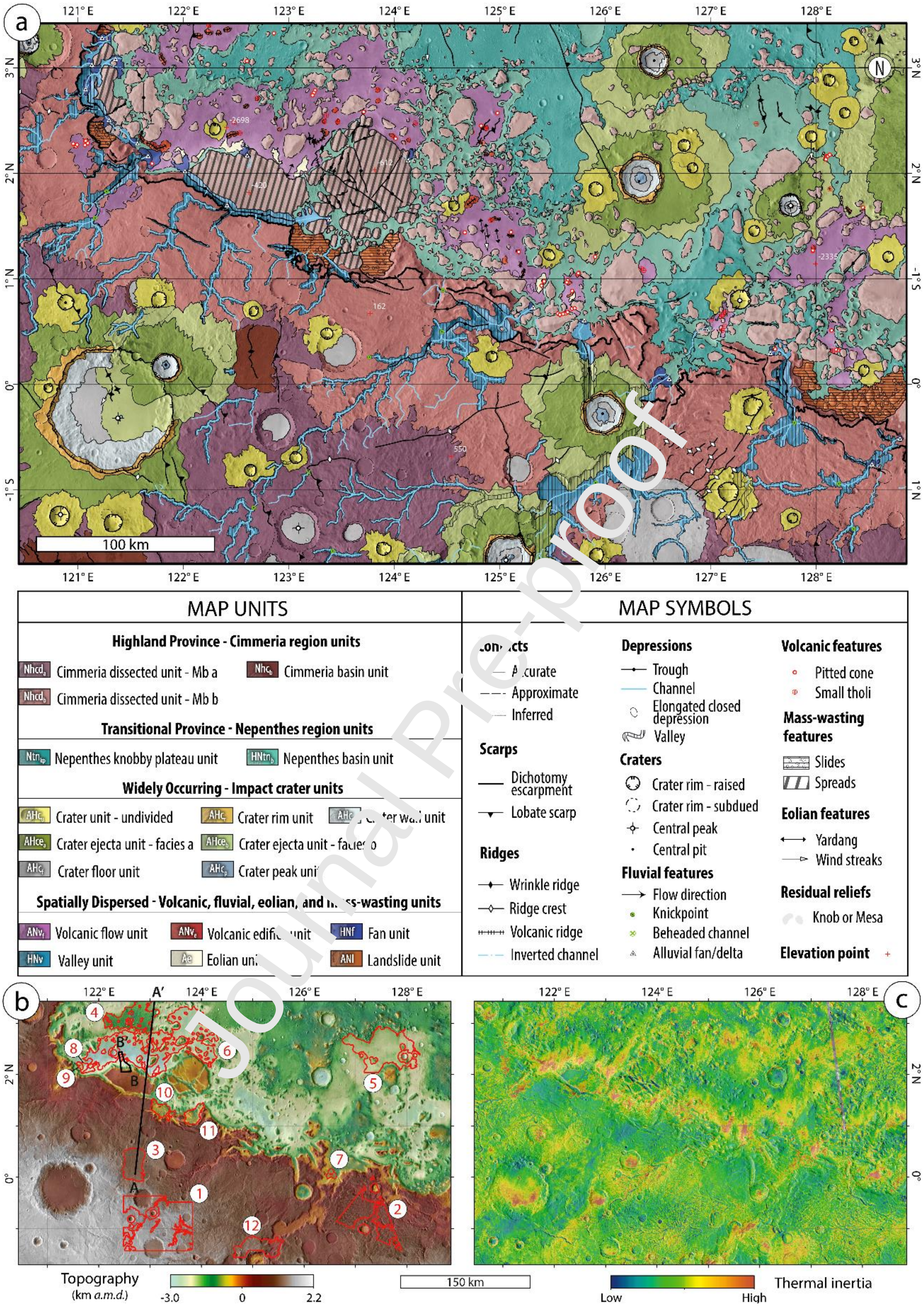

Fig. 2. (a) Geologic-geomorphic map of the CNTZ showing the geologic units and the identified morphological and tectonic features over a THEMIS-IR day mosaic. A high-resolution version of the map is available in Supplementary Material. (b) Colorized

elevation model of the study area from HRSC-MOLA blended data over a mosaic of THEMIS-IR day images. Red polygons represent the crater-counting areas (1 to 12) selected for dating the main units (Fig. 8). The black line indicates the trace of the SHARAD profile “S_02596802” (Fig. 9) and that of the geological cross-section (A-A’) shown in Fig. 11. The black polygon depicts the area covered by the bock diagram (Fig. 13) that interprets the subsurface geology along the B-B’ profile. (c) Qualitative TI mosaic of the study area derived from THEMIS over a mosaic of THEMIS-IR day images.

The Cimmeria basin unit (Nhc_b) corresponds to depressions of uncertain origin inset into member ‘a’ and filled with sediments. It shows a smoother and less-cratered surface than those of the Cimmeria dissected units, pervasive wrinkle ridges, and absence of valleys.

The Nepenthes region units comprise the Nepenthes knobby plateau unit (Ntn_{kp}) and the Nepenthes basin unit ($HNtn_b$) (Fig. 2a). The Nepenthes knobby plateau unit (Ntn_{kp}) crops out in the inter-crater plateau areas of Nepenthes Mensae. This moderately cratered unit features knobby terrains formed by degraded residual hills carved in materials of the unit $Nhcd_b$ and mass-wasted materials that form aprons around degraded reliefs (e.g., Tanaka et al., 2005). The unit also displays NW-SE-oriented lobate scarps and widely distributed eolian erosional landforms such as yardangs with a prevailing NW-SE orientation (see detail in Fig. 3a).

The Nepenthes basin unit ($HNtn_b$) corresponds to low-lying areas and the associated slopes of the Nepenthes Mensae region located between mesas and knobs, as well as on floors of ancient and highly degraded impact basins (see Fig. 1b). Depressions in

Nepenthes Mensae show lines of evidence of being enclosed paleolake basins, such as the occurrence of putative Gilbert-type deltas and paleoshore platforms (Rivera-Hernández and Palucis, 2019; García-Arnay and Gutiérrez, 2020). The Nepenthes basin unit is characterized by lower crater density than unit $\mathrm{Ntn_{kp}}$, and relatively smooth surfaces locally interrupted by wrinkle ridges, as well as small tholi and pitted cones (see Fig. 3b). The boundary between units $\mathrm{HNtn_b}$ and $\mathrm{Ntn_{kp}}$ is gradational.

Seven impact crater units have been differentiated on the basis of their morpho-structural components (i.e., rim, wall, floor, peak, and ejecta), following the classification proposed by Skinner and Tanaka (2018). The crater unit undivided ($\mathrm{AHc_u}$) includes well-preserved craters with rim diameter ranging between 5 and 13 km and the associated materials. This unit shows lobate ejecta morphologies, commonly hummocky crater floor, and scarce occurrence of central peak or pit. The rest of the impact crater units were ascribed to moderately to well-preserved impact craters with rim diameters ≥13 km. The crater peak unit ($\mathrm{AHc_p}$) was mapped at or next to the center of impact craters. It is characterized by mounds with irregular and grooved surfaces, and the common presence of central pits. The crater floor unit ($\mathrm{AHc_f}$) occurs between the foot of the crater wall and the central peak, and displays smooth, near-planar surfaces. Central peaks can be absent, and pits may occur in the center of the crater. The crater wall unit ($\mathrm{AHc_w}$) was mapped between the crater floor and rim units. This rough, and locally rugged unit is characterized by scarps, blocks, rockfalls and locally discontinuous terraces. The rim crater unit ($\mathrm{AHc_r}$) is located along the continuous to discontinuous crested rim. It is characterized by an inward-facing steep scarp frequently dissected by gullies and grooves. The crater ejecta units are divided into two morpho-facies. The crater ejecta unit–facies a ($\mathrm{AHce_a}$) represents the proximal deposits. It is characterized by multiple overlapping rugged lobes with flowbands. The crater ejecta unit–facies b (AHce$_b$) is the outer unit, formed by multiple overlapping smooth flow-oriented lobes.

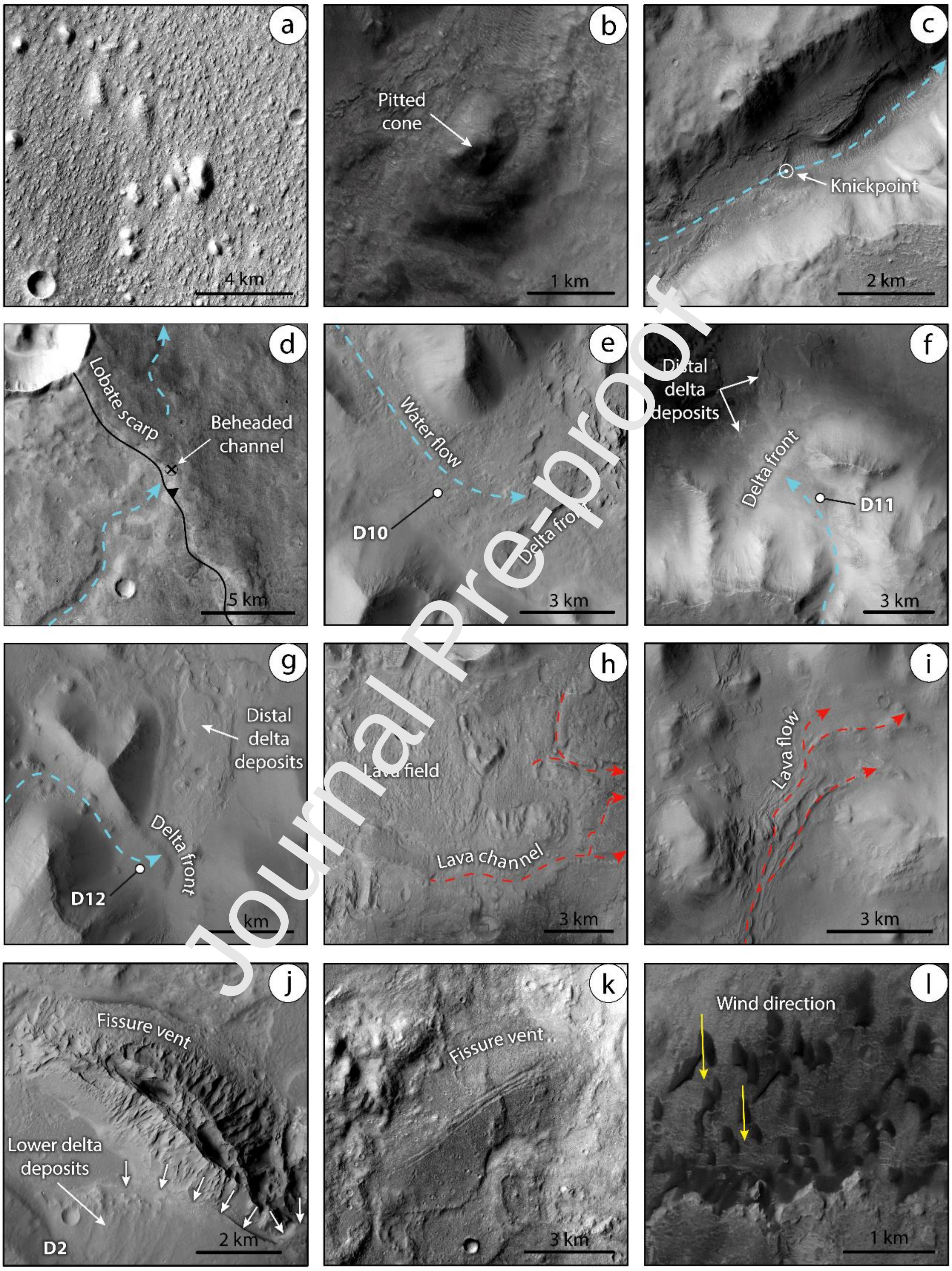

Fig. 3. CTX images illustrating remarkable geomorphic features in the study area (locations indicated in Fig. 1a). (a) A detail of the knobby terrain that characterizes the

Nepenthes knobby plateau unit (Ntn$_{kp}$). Note the presence of elongated erosional landforms with roughly parallel orientation ascribable to yardangs and wind-deflated surfaces. (b) Putative volcanic edifices such as pitted cones. (c) Fluvial valley showing a sharp break in the longitudinal profile (i.e., knickpoint). (d) Defeated and beheaded channel sections separated by a lobate scarp, attributable to a surface-rupturing thrust fault that disrupted the drainage. (e, f, g) Fan-shaped deposits attributable to putative Gilbert-type deltas (labelled as D# in our putative delta and alluvial fan catalogue presented in section 4.1). Other putative volcanic features such as lava fields, flows and channels (h, i), as well as fissure vents (j, k). White arrows in (j) indicate the lower putative delta deposits of "D2" locally overlying those at the foot of the fissure vent and surrounding plains. (l) Barchan dune fields indicating a dominant southeast-directed wind, as indicated by yellow arrows. North is up in all cases.

Six locally distributed units have been mapped. The valley unit (HNv) corresponds to valleys carved in the Cimmeria region units Nhcd$_a$ and Nhcd$_b$, and rarely in the Nepenthes knobby plateau unit (Ntn$_{kp}$). This unit is characterized by high-TI, smooth deposits underlying the floors of valley networks with dendritic or trellis pattern. Licus Vallis, which is the longest, widest, and deepest valley in the study area, shows an apparently poorly evolved watershed, as suggested by its convex hypsometric curve and a very low drainage density (García-Arnay et al., 2018b). Valley floors, generally characterized by a low THEMIS TI related to the presence of eolian deposits (see Fig. 2c), often show knickpoints (Fig. 3c) and rarely preserved incised or inverted channels. The degree of entrenchment of the valleys increases towards the dichotomy boundary, next to the paleolakes that controlled the position of the base level during their development, as indicates the presence of putative Gilbert-type deltas (e.g., García-

Arnay and Gutiérrez, 2020). Some valleys are locally buried by ejecta deposits or disrupted by lobate scarps resulting in the formation of defeated and beheaded channels sections (see Fig. 3d).

Table 1. Characteristics of the fan-shaped features (identified as D# and F# for putative deltas and alluvial fans, respectively) recognized within and near the study area, as well as their associated basins. The front elevation for the stepped fans corresponds to the slope-break of the uppermost step. Features from D1 to D9 match with those referred by García-Arnay and Gutiérrez (2020). The basin type can be open (O) or closed (C). "N/A" = Not applicable.

ID	Latitude (N)	Longitude (E)	Front elevation (m)	Visible layering	Multi-lobate	Morphology	Basin type	First reference
D1	3°5'31"	121°20'54"	-1865	✓	✓	Stepped	C	García-Arnay et al. (2018a)
D2	2°10'11"	121°39'29"	-1952	✓	✓	Stepped	C	Irwin et al. (2005)
D3	2°1'28"	122°00'31"	-1935	✓	✓	Stepped	C	García-Arnay et al. (2018a)
D4	1°34'7"	123°22'52"	-1793	✓	✓	Continuous	C	García-Arnay et al. (2018a)
D5	0°44'6"	125°18'55"	-1920	✓	✗	Continuous	C	García-Arnay et al. (2018a)
D6	0°36'33"	125°47'50"	-1975	✓	✗	Continuous	C	García-Arnay et al. (2018a)
D7	0°3'14"	126°36'20"	-1186	✓	✓	Continuous	O	García-Arnay et al. (2018a,b)
D8	0°31'21"	126°58'19"	-1920	✓	✓	Continuous	C	García-Arnay et al. (2018a)
D9	0°18'8"	127°34'00"	-1783	✓	✓	Continuous	C	García-Arnay et al. (2018a)
D10	2°17'19"	121°33'25"	-2370	✓	✓	Continuous	C	This study
D11	2°10'26"	122°35'59"	-1906	✓	✓	Stepped	C	This study
D12	2°7'41"	124°7'40"	-1872	✓	✓	Stepped	C	This study
F1	-2°12'6"	120°57'9"	N/A	✗	✗	Continuous	O	This study
F2	2°48'16"	121°3'56"	N/A	✓	✓	Continuous	C	Rivera-Hernández and Palucis (2019)
F3	-1°55'21"	121°7'59"	N/A	✗	✓	Continuous	O	This study

F4	3°2'10"	121°7'28"	N/A	✓	✓	Continuous	C	Rivera-Hernández and Palucis (2019)
F5	3°17'25"	121°13'19"	N/A	✓	✓	Stepped	C	Rivera-Hernández and Palucis (2019)
F6	2°30'38"	121°17'13"	N/A	✓	✓	Stepped	C	Rivera-Hernández and Palucis (2019)
F7	1°42'6"	122°24'33"	N/A	✓	✗	Continuous	O	Rivera-Hernández and Palucis (2019)
F8	-2°59'40"	122°41'9"	N/A	✓	✓	Continuous	O	This study
F9	-4°10'27"	125°56'16"	N/A	✗	✓	Continuous	O	This study
F10	-0°45'21"	128°31'51"	N/A	✓	✓	Continuous	O	This study
F11	-0°30'47"	128°47'51"	N/A	✓	✓	Continuous	O	This study
F12	-1°11'53"	129°52'23"	N/A	✓	✓	Stepped	O	This study

The fan unit (HNf), which is laterally associated with unit HNv, occurs at the mouth of the valleys, generally along the foot of the dichotomy. This unit corresponds to fan-shaped deposits with generally smooth surfaces, but sometimes corrugated due to differential erosion on layered sediments. Some fans show different lobes and rare channels carved into the surface (see Fig. 3e-g, and Fig. 3 from García-Arnay and Gutiérrez (2020)). The frontal slope of the fans can be continuous or stepped. Due to the paleoenvironmental interest of unit HNf, we present an updated catalogue of fan-shaped deposits identified within and near the study area in Table 1.

The volcanic flow unit (ANv_f) shows poorly cratered, uneven, and smooth to rugged surfaces with frequent grooves, channels (Fig. 3h), and overlapping lobes (Fig. 3i). This unit, which is darker in THEMIS daytime IR images than the surrounding plains, occurs in the deeper areas of the depressions of Nepenthes Mensae, and locally in the highland province near the dichotomy. It is locally modified by NE-SW-striking wrinkle ridges, NW-SE-aligned erosional eolian landforms such as yardangs, as well as small elongated closed depressions. This unit locally overlies units $Nhcd_b$ and $HNtn_b$, locally also underlies unit HNf, and grades into unit ANv_e.

The volcanic edifice unit (ANv_e) is characterized by sloping, and rugged to smooth surfaces with isolated and coalesced fissures (see Figs. 3j, k), as well as small cone- and mound-shaped features (Fig. 3b). Cones and mounds often show small knobs and/or pits at their summit. Overlapping lobes related to the volcanic flow unit (ANv_f) seem to emanate from raised fissures, cones, and mounds.

The eolian unit (Ae) often consists of dune fields that mainly occur in the southern sector of the depressions of Nepenthes Mensae, near the foot of the dichotomy escarpment. This unit, which shows dark tones in CTX panchromatic images and bright tones in THEMIS daytime IR images, is formed by fields of barchan and longitudinal dunes indicating a dominant southeast-directed wind (see Figs. 1b and 3k). It locally overlies units ANv_f, $HNtn_b$ and $Nhcd_b$.

The landslide unit (ANl) usually occurs associated with the ca. 2 km high dichotomy escarpment. It is characterized by rugged, rolling, and hummocky terrains with intervening large blocks that can be carved by channels (see details in the 3D image in Fig. 12). Locally, this unit overlies units $Nhcd_b$ and $HNtn_b$.

4.1.2 Geomorphology

We have also mapped the main geomorphic features in the CNTZ (Fig. 2a). Two types of scarps have been identified: lobate scarps, and those associated with the dichotomy boundary. Lobate scarps are ridge-like, linear to sinuous landforms in planview that display asymmetric cross profiles with convex and steep scarp faces (e.g., Watters and Robinson, 1999; Skinner and Tanaka, 2018), up to ~250 m high in the study area (Fig. 3d). These landforms mostly occur in the Cimmeria dissected units ($Nhcd_a$ and $Nhcd_b$) and the Nepenthes knobby plateau unit (Ntn_{kp}), showing a prevalent NW-SE orientation with often SW-facing scarps. In some cases, lobate scarps disrupt valleys and pre-existing crater floors (see locations at 0°48'11"S, 125°5'23"E; 0°0'25"N, 122°53'45"E and 1°29'17"S, 128°0'17"E), or appear interrupted by gaps related to impact craters that locally obliterated them. We mapped 22 lobate scarps that range in length from 4.5 to 103.1 km (27.7 km mean, 21.5 km median).

The dichotomy boundary displays a linear to sinuous escarpment ca. 2 km high that is dissected by numerous valleys, which often display conspicuous knickpoints. This major escarpment exhibits a dominant NW-SE orientation that turns to a N-S trend west of the map and occurs in member b of the Cimmeria dissected unit ($Nhcd_b$). The foot of the escarpment generally defines the contact between the highland and transition units throughout the CNTZ. Gullies are common, as well as hummocky terrains with intervening large blocks associated to the landslide unit (ANl). We mapped 36 escarpment segments separated by valleys with a cumulative mapped length of 751.6 km.

Four types of negative relief features have been differentiated: valleys, channels, elongated closed depressions, and troughs. Valleys are networks of V-shaped, elongate, steep-walled depressions with linear to sinuous trace and dendritic to trellis pattern (Fig. 4a, b). Valley networks often exhibit a pattern apparently controlled by lobate scarps, ridge crests and troughs. Some valleys disrupted by lobate scarps show evidence of later adaptation to these landforms, such as deflections. Their associated deposits comprise the valley unit (HNv) (see section 4.1.1). We mapped 32 valley networks within the map region that range in planimetric area from 6.9 to 2,400.7 km^2 (324.5 km^2 mean).

Channels are elongate, narrow, and shallow depressions with linear to sinuous trace that occur in the valley floors and join in the downslope direction (e.g., Sharp and Malin, 1975) (see Fig. 4a, b). Channels associated to the valley unit (HNv) mostly occur in the Cimmeria dissected units (Nhcd$_a$ and Nhcd$_b$), and rarely in the Nepenthes knobby plateau unit (Ntn$_{kp}$). They locally display positive relief sections forming channel ridges related to relief inversion by differential erosion. Watersheds in the CNTZ are characterized by streams of up to fourth order using the Strahler's classification (Strahler, 1952), such as that of Licus Vallis (e.g., García-Arnay et al., 2018b). The channel network in the vicinity of the dichotomy tends to show a rectangular pattern, with channel sections following a dominant NE-SW trend and a secondary NW-SE orientation, probably controlled by fractures. We have mapped 248 channels in the study area ranging in length from 0.07 to 143.6 km (16.1 km mean, 10.3 km median).

Elongated closed depressions are depressions that commonly exhibit well-defined scarped boundaries (e.g., Parenti et al., 2020) (see Fig. 4c). These landforms locally occur in the volcanic flow unit (ANv$_f$), display major axes ranging from 10s to ~700 m, and a prevalent NW-SE trend that coincides with that of nearby yardangs, dunes, and wind streaks. Some of these depressions frequently display sharper and steeper NW margins, whereas the SE edges show gentler slopes, with poorly defined boundaries, which is also observed in depressions produced by deflation (e.g., blowouts). The current wind regime, acting more intensively on their SE side, has probably caused reshaping and enlargement of the depressions, and eventually leading to their coalescence.

Troughs are rectilinear or slightly arcuate steep-walled depressions with maximum depths and widths of 1 and 7 km, respectively. These landforms are located along the northern Terra Cimmeria in the vicinity of the dichotomy escarpment, mainly cut into member b of the Cimmeria dissected unit (Nhcd$_b$) and into residual reliefs of this unit in

Nepenthes Mensae to form fretted valleys (see Fig. 5a). Troughs show a dominant NW-SE orientation and a secondary NE-SW trend, forming a distinctive polygonal pattern (Fig. 5b). We identified and mapped 72 troughs that range in length from 4.0 to 49.4 km (17.4 km mean, 13.7 km median).

Four types of ridges were mapped: wrinkle ridges, ridge crests, inverted channels, and volcanic ridges (Fig. 2a). Wrinkle ridges are linear to curvilinear ridges with asymmetric transverse profile, whose crests are characterized by complex crenulations colloquially called "wrinkles" (e.g., Watters, 1988) (see Fig. 4d). In our map these landforms display two dominant orientations: a NW-SE trend that occurs in the plains of the basin units of the Cimmeria and Nepenthes regions (Nhc_b and $HNtn_b$, respectively), and a NE-SW orientation within the volcanic flow unit (ANv_f). These crenulated ridges, which generally rise up to ~50 m above surrounding plains, commonly show the maximum width in the middle section. We mapped 18 wrinkle ridges ranging in length from 5.3 to 35.2 km (13.3 km mean, 9.4 km median).

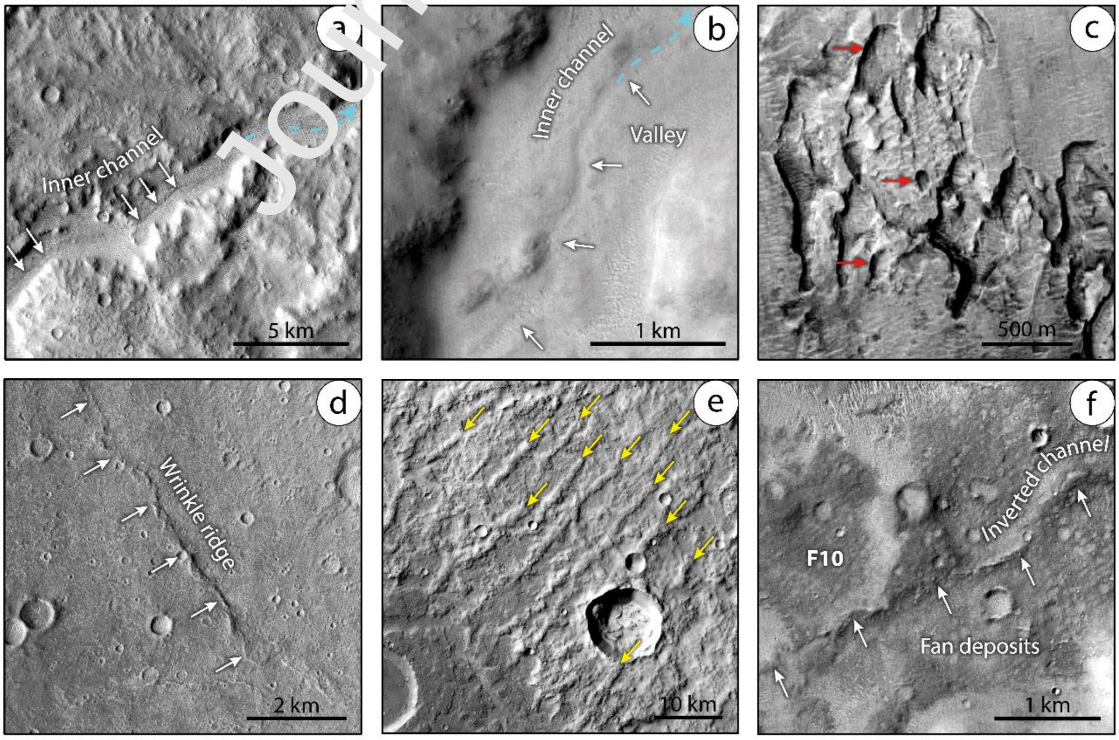

Fig. 4. CTX images illustrating remarkable ridges and negative relief features in the study area (locations indicated in Fig. 1a). (a, b) Inner channels within ancient valleys, as indicated by white arrows. Blue arrows indicate the paleoflow of the inner channel. (c) Elongated closed depressions exhibiting well-defined scarped boundaries (red arrows). (d) NW-SE-oriented wrinkle ridge, as shown by white arrows, occurring in the plains of the basin unit of the Nepenthes region (unit $\mathrm{HNtn_b}$). (e) Ridge crests with a dominant NE-SW orientation, as indicated by yellow arrows, forming a conspicuous swarm with subparallel pattern. (f) Fan-shaped deposits attributable to a putative alluvial fan (labelled as F# in our putative delta and alluvial fan catalogue presented in section 4.1) exhibiting a possible inverted channel with sinuous pattern in planview, as shown by white arrows. North is up in all cases.

Ridge crests, also called high-relief ridges, are characterized by a near symmetrical transverse profile and higher relief than the wrinkle ridges (e.g., Watters et al., 2009) (see Fig. 4e). These features mostly occur in the Cimmeria dissected units ($\mathrm{Nhcd_a}$ and $\mathrm{Nhcd_b}$) displaying lateral continuity across them. Although orientations vary across the map, ridge crests exhibit a dominant NE-SW orientation, and a secondary NW-SE strike. The conspicuous swarm with subparallel pattern east of the map (around -1ºN, 127ºE; see Fig. 4e) is interrupted at an ancient and degraded impact crater 60 km in diameter, indicating an older age for the ridges (see Fig. 2a). We have mapped 28 ridge crests that range in length from 1.5 to 86.3 km (16.6 km mean, 11.5 km median).

Channel ridges related to relief inversion, commonly known as “inverted channels”, are characterized by ridges with sinuous pattern in planview (e.g., Burr et al., 2010; Hayden et al., 2019; Clarke et al., 2020; Dickson et al., 2021) (see Fig. 4f). In the map region we have identified sinuous ridges up to 3.8 km in length associated with the fan unit (HNf) that occurs in the eastern sector of the map area, specifically on the fan-shaped deposit F10 (see Table 1 and Fig. 4f).

Volcanic ridges correspond to raised fissure vents that occur in the volcanic edifice unit (ANv$_e$). These linear to curvilinear ridges reach up to ~600 m in local relief, exhibit pits and/or elongated depressions at the top, and smooth to rugged slopes carved by grooves and gullies (see Fig. 3j, k, and Fig. 5c). The orientation of the volcanic ridges shows a rather scattered distribution, with weak NW-SE and NE-SW prevalent trends (Fig. 5d). We have mapped 21 volcanic ridges ranging in length from 1.1 to 12.5 km (4.4 km mean, 3.8 km median).

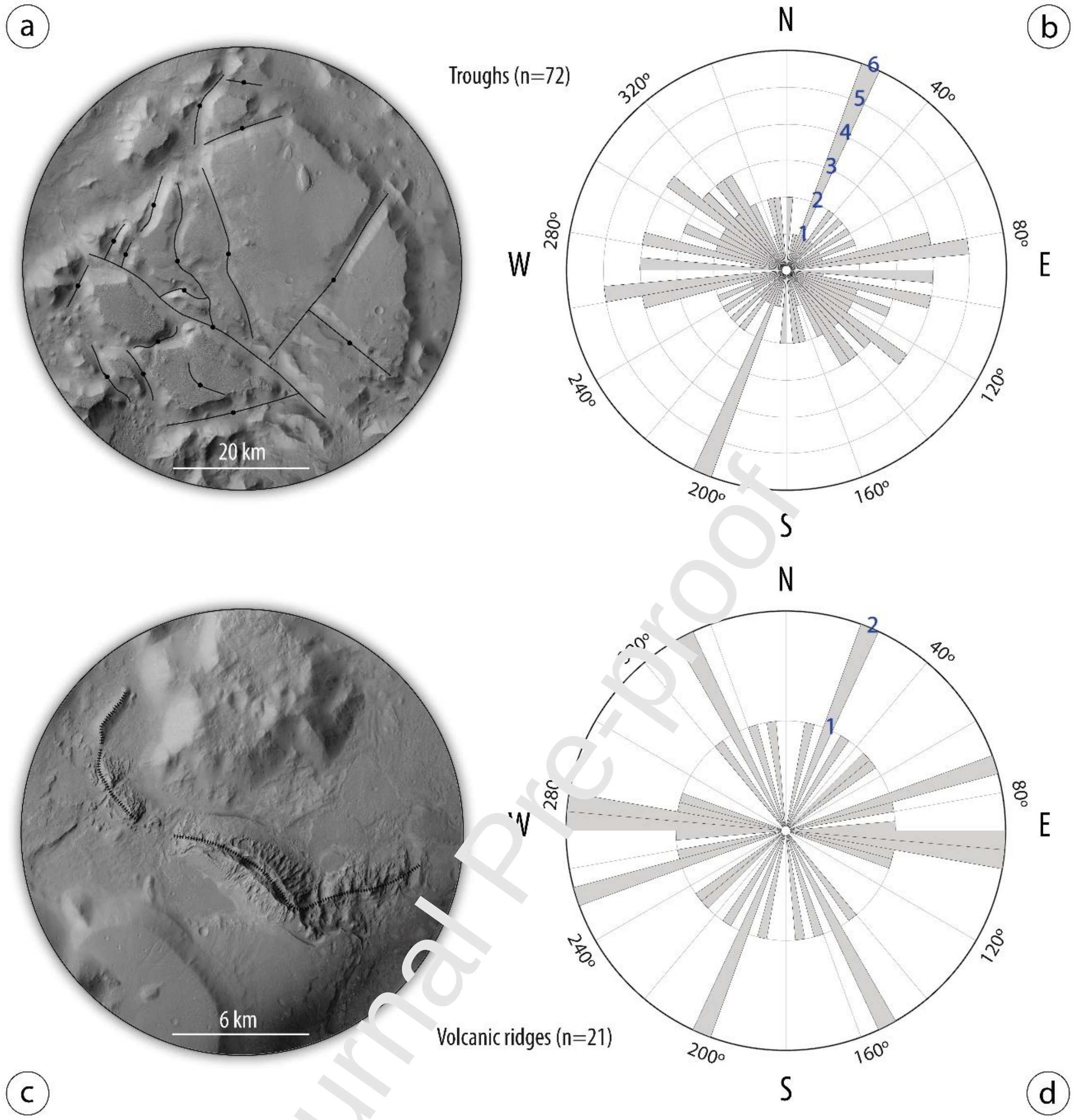

Fig. 5. (a, c) Examples of troughs and volcanic ridges, respectively (CTX image mosaic; North is up). (b, d) Rose diagrams showing the distribution of the orientation of troughs and volcanic ridges, respectively. Note that the orientation of volcanic ridges displays higher dispersion than the troughs. Their higher dispersion may be partially due to the lower number of features (n).

Two types of cone- and mound-shaped landforms were identified within the volcanic edifice unit (ANv$_e$): pitted cones and small tholi. Pitted cones are conical hills with circular outline in planview and smooth slopes that exhibit a central pit in their summit (e.g., Skinner and Tanaka, 2018) (see Fig. 3b). These landforms occur either isolated or aligned, mainly associated with the volcanic flow unit (ANv_f), and less commonly in the Nepenthes knobby plateau and Nepenthes basin units (Ntn_{kp} and $HNtn_b$, respectively). We have identified and mapped 47 pitted cones within the study area, ranging in diameter from 200 m to 1.2 km.

Small tholi are mounds with subtle slopes bounded by marginal scarps, and often showing central peaks (e.g., Skinner and Tanaka, 2018). These mounds of up to 2.7 km in diameter are frequently isolated, but in some cases form clusters. They generally occur associated with the volcanic flow unit (ANv_f), and rarely in the Nepenthes basin unit ($HNtn_b$). We mapped 30 small tholi in the map region.

4.2 Mineral composition of units of paleoenvironmental interest

The spectral analysis of the CRISM scenes FRT00017610 (~18 m/pixel, ~10x10 km) and HRL000134F5 (~36 m/pixel, ~10x20 km) was carried out in order to determine the composition of the surface material in two different areas of the CNTZ with paleoenvironmental interest. These CRISM observations (Figs. 6a and 7a) include fan-shaped deposits, and spatially associated distal fan deposits and surrounding plains (see locations in Fig 1). The layered fan-shaped deposits (unit HNf) shown in Fig. 6a occur within the landform identified as “D2” in Table 1. It is in the western sector of the study area at the mouth of a canyon-type valley and was interpreted as a putative delta for the first time by Irwin et al. (2005), displaying a stepped morphology (upper and lower fan). The PHY spectral parameter map (Fig. 6b) suggests the presence of two clay-bearing compositional units in the lower fan deposits: (1) laterally continuous patches of hydrated Fe/Mg-phyllosilicates occurring at different stratigraphic levels, which are the most common hydrated minerals on Mars (Carter et al., 2013); and (2) smaller isolated patches of hydrated Al-smectites and/or hydrated silica, shown by pink- and cyan-colored pixels, respectively (Fig. 6b). Aluminum smectites and/or hydrated silica occur in light-toned layered materials, as revealed by the HiRISE image ESP_016547_1820 (close-up view in Fig. 6a). The ratioed I/F spectra (i.e., s1/s2) for both inferred compositional units reveal two sharp absorption bands at ~1.5 and ~2.0 μm, probably related to the occurrence of crystalline water ice on the surface or in the atmosphere (e.g., Brown et al., 2010; Cull et al., 2010; Viviano-Beck et al., 2014). The ratioed spectra also show a subtler absorption band at ~1.4 μm, probably related to structural H_2O and OH. In contrast, the ~1.9 μm absorption band related to structural H_2O is probably masked by the bandwidth associated with the water-ice absorption band at ~2.0 μm (see Fig. 6c, d). Furthermore, these ratioed spectra exhibit subtler absorption bands at ~2.31 and ~2.39 μm (Fig. 6c), and at ~2.2 μm (Fig. 6d) related to Fe/Mg- and Al/Si-OH bonds, respectively (Ehlmann et al., 2009; Viviano-Beck et al., 2014). These absorption bands, together with those related to OH/H_2O bonds, allow inferring the occurrence of hydrated Fe/Mg phyllosilicates (Fig.

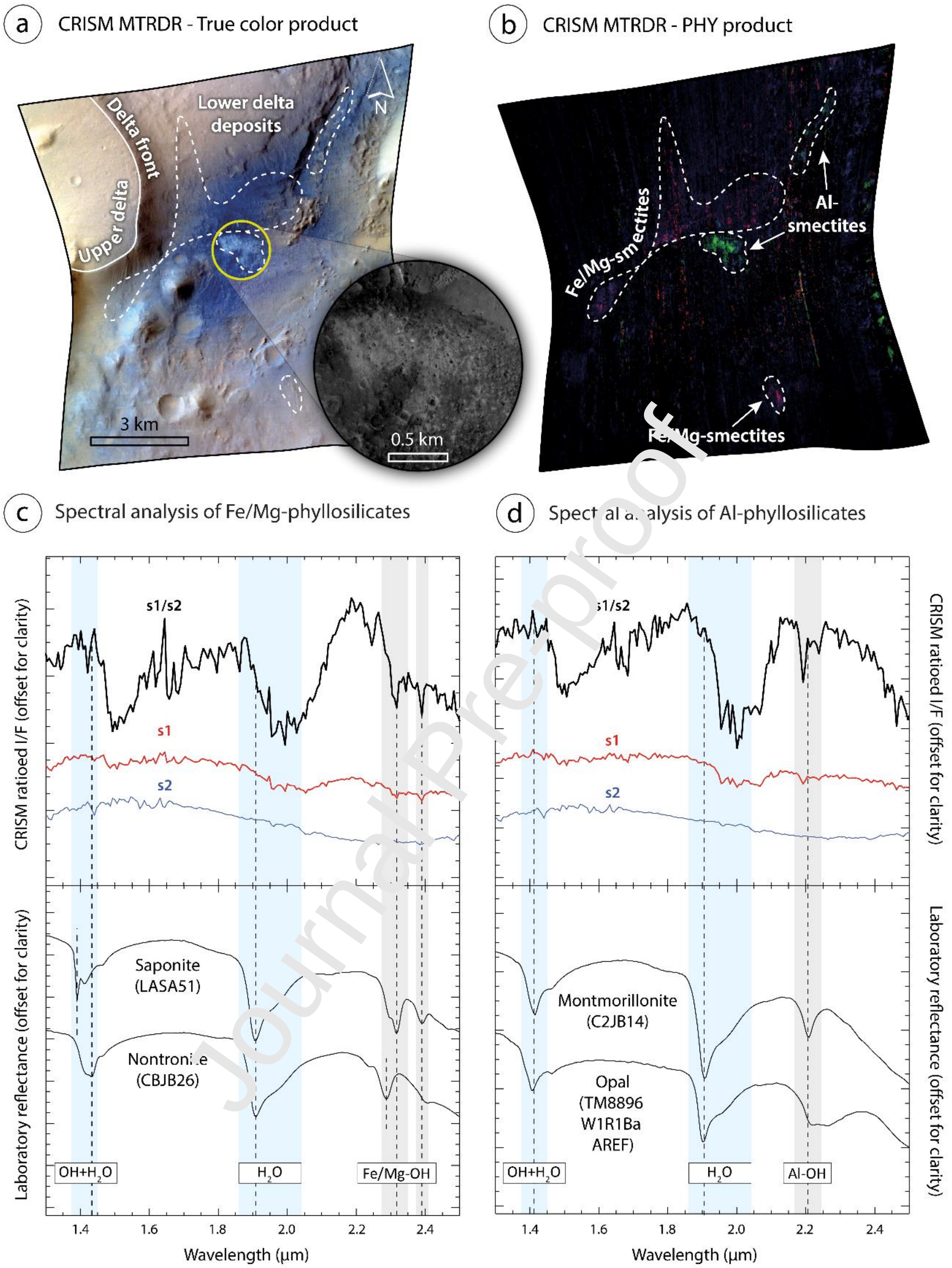

Fig. 6. (a) True color product of the CRISM map-projected scene "FRT00017610" (see location in Fig. 1a). The close-up view shows a detail of the light-toned surfaces associated with the lower fan environment (HiRISE image ESP_016547_1820). (b) Phyllosilicate spectral parameter map (PHY product) generated for the same scene. Pink and cyan tones indicate the presence of hydrated Fe/Mg-smectites, and hydrated Al-

smectites/hydrated silica, respectively. (c, d) CRISM ratioed I/F spectra (i.e., s1/s2) for hydrated Fe/Mg-smectites and hydrated Al-smectites/hydrated silica (above), compared to laboratory spectra (below). Vertical dashed lines indicate diagnostic absorption band depths, and blue and grey bands represent bandwidths for OH/H_2O, as well as Fe/Mg-OH and Al/Si-OH, respectively.

6c), hydrated Al-rich smectites and/or hydrated silica (Fig. 6d), as well as crystalline H_2O ice on the surface or in the atmosphere. Accordingly, the observed diagnostic features can be consistent with the presence of saponite (Mg-rich smectite) and nontronite (Fe-rich smectite) in the Fe/Mg-smectite unit, and montmorillonite (Al-rich smectite) and/or opal (hydrated silica) in the Al-smectite/hydrated silica unit, as indicated by the comparison between the ratioed spectra and those from the CRISM/ENVI spectral library (Viviano-Beck et al., 2015).

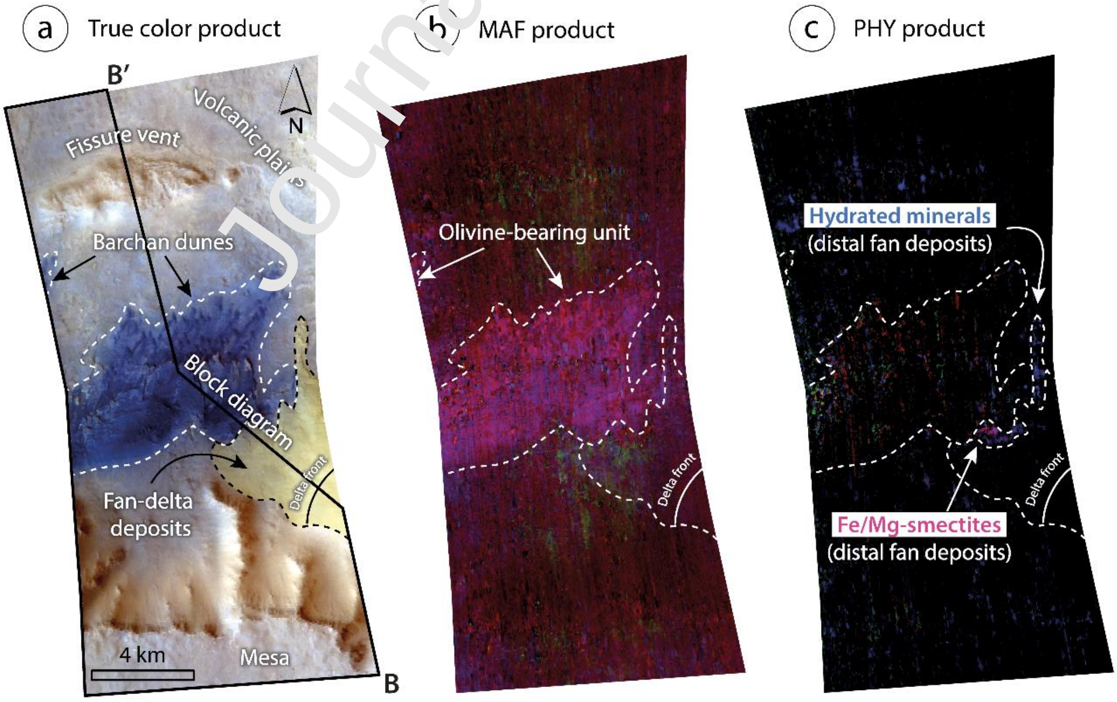

Fig. 7. (a) True color product of the CRISM map-projected scene “HRL000134F5” (see

location in Fig. 1a). The black-lined polygon indicates the area covered by the block diagram shown in Fig. 13, which shows an interpretation for the subsurface geology along the B-B’ profile. (b, c) Mafic mineralogy and phyllosilicate spectral parameter maps (MAF and PHY products, respectively) for the same scene. Note the spatial association between clay- and olivine-bearing deposits around the distal fan environment.

The fan-shaped deposits shown in Fig. 7a, labelled as “D1F” in Table 1, are located at the mouth of a short valley (see details in Fig. 3f). The MAF and PHY spectral parameter maps indicate, respectively, extensive olivine-bearing deposits associated with the barchan dune field of the unit Ae (Fig. 7b), and patches of ferromagnesian phyllosilicates occurring along the distal fan deposits (unit HNf) with undetermined hydrated minerals (Fig. 7c). Cartographic relationships indicate that the distal fan deposits overlay the surrounding plains that form part of unit ANv_f, and are locally covered by the olivine-rich dark dunes.

4.3 Estimation of surface ages

The analysis of the crater size- frequency distribution (SFD) was performed in 12 counting areas representing the main map units, in order to obtain their model age (Fig. 8). We selected, where possible, crater-counting areas larger than 1,000 km^2 to minimize the impact of the local pattern variations in cratering (e.g., Warner et al., 2015). For clarity, the units have been grouped by regions and/or according to their spatial distribution, and ages have been ordered from older to younger.

In the Cimmeria region, we obtained average age estimates (red fit lines) of 4.00 ±

0.04/0.06 Ga (Early to Middle Noachian), and 3.89 ± 0.03/0.04 Ga (Middle Noachian) for the Cimmeria dissected units $Nhcd_a$ and $Nhcd_b$, respectively, as well as 3.62 ± 0.02/0.02 Ga (Late Noachian) for the Cimmeria basin unit (Nhc_b), considering counting areas of ~4,600, ~1,800 and ~790 km^2, respectively (Fig. 8a-c). In these diagrams we identified several kinks that suggest resurfacing events affecting to km-sized and smaller craters (blue and green fit lines), such as the large kink that occurs in the SFD shown in Fig. 8a at D <3 km, with a resulting average age of the resurfacing event of 3.36 ± 0.02/0.02 Ga (Late Hesperian).

In the Nepenthes region, we estimated surface ages of 3.76 ± 0.03/0.04 Ga (Late Noachian) and 3.63 ± 0.05/0.08 Ga (Late Noachian to Early Hesperian) for the Nepenthes knobby plateau unit (Ntn_{kp}) and the Nepenthes basin unit ($HNtn_b$), with counting areas of ~1,200 and ~2,400 km^2, respectively (Fig. 8d, e).

Among the spatially dispersed units, we estimated the surface ages for the fan unit (HNf), the volcanic flow unit (ANv_f), and the landslide unit (ANl). For the fan unit (HNf), we selected three counting areas located in the largest fan-shaped deposits to reduce the potential impact of: (1) the spatial variability in cratering processes; and (2) the exclusion of larger craters associated with smaller counting areas (Warner et al., 2015). Thus, we obtained average ages of 3.64 ± 0.04/0.07 Ga (Late Noachian) for putative delta “D7” (see Table 1), and 3.63 ± 0.10/0.31 Ga (Late Noachian to Late Hesperian; lower fan) and 1.99 ± 0.36/0.36 Ga (Early Amazonian; upper fan) for putative delta “D2” (Fig. 8g-i), with counting areas of ~85.4, ~53, and ~41.1 km^2, respectively. For the volcanic flow unit (ANv_f), a fit to the D >450 m crater population provided an age estimate of 1.83 ± 0.17/0.17 Ga (Early Amazonian) (Fig. 8f), considering a counting area of ~9,000 km^2. Finally, we considered two counting areas for the landslide unit (ANl) of ~318 and ~314

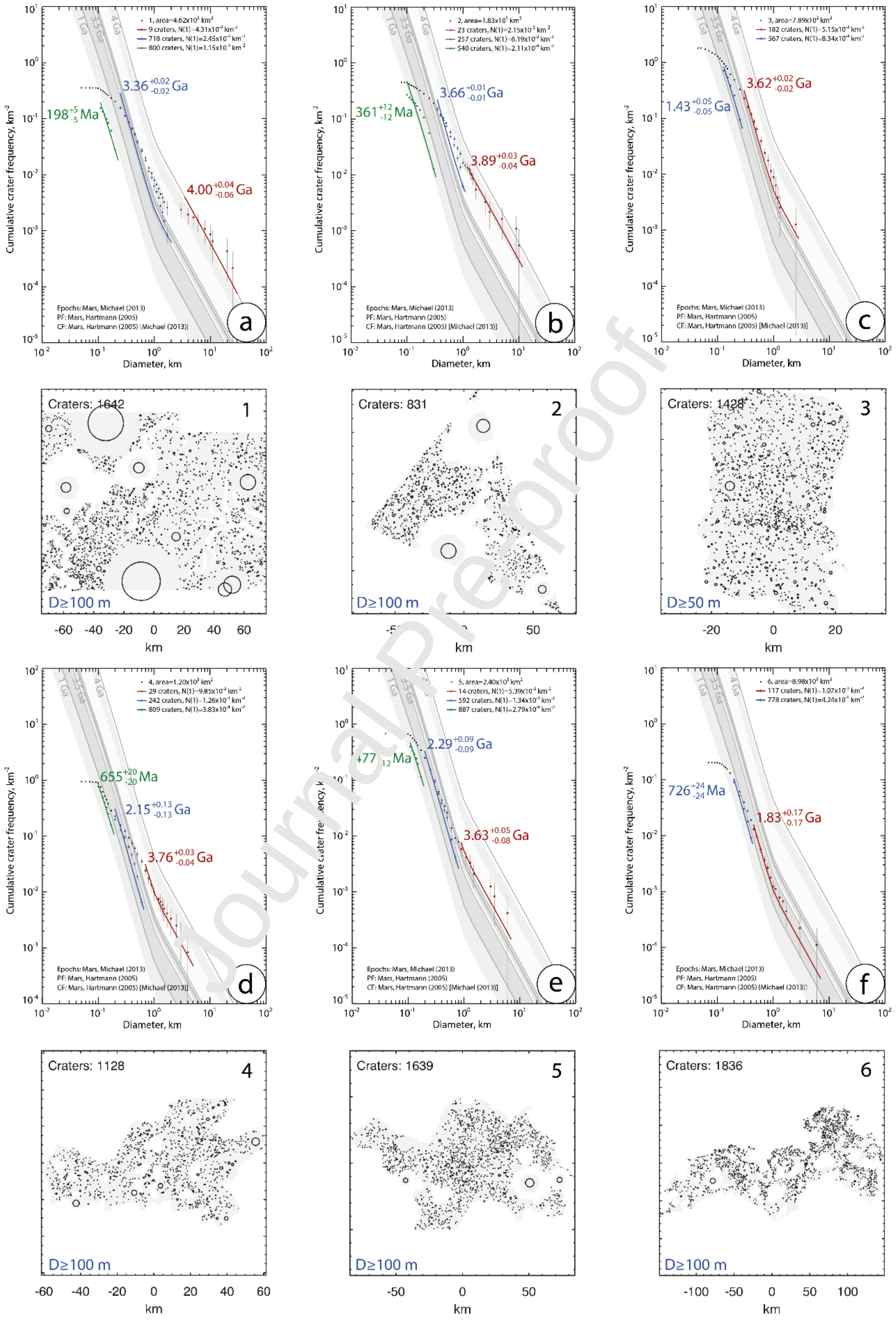
1 Ga
3.5 Ga
4 Ga
1, area=4.62x10³ km²
9 craters, N(1)=4.31x10⁻² km⁻²
718 craters, N(1)=2.45x10⁻³ km⁻²
800 craters, N(1)=1.15x10⁻⁴ km⁻²
3.36 +0.02 -0.02 Ga
198 +5 -5 Ma
4.00 +0.04 -0.06 Ga
Epochs: Mars, Michael (2013)
PF: Mars, Hartmann (2005)
CF: Mars, Hartmann (2005) [Michael (2013)]
a
Cumulative crater frequency, km⁻²
Diameter, km
10⁻² 10⁻¹ 10⁰ 10¹ 10²
2, area=1.83x10³ km²
23 craters, N(1)=2.15x10⁻² km⁻²
257 craters, N(1)=6.19x10⁻³ km⁻²
540 craters, N(1)=2.11x10⁻⁴ km⁻²
3.66 +0.01 -0.01 Ga
361 +12 -12 Ma
3.89 +0.03 -0.04 Ga
b
3, area=7.89x10² km²
182 craters, N(1)=5.15x10⁻³ km⁻²
567 craters, N(1)=8.34x10⁻⁴ km⁻²
3.62 +0.02 -0.02 Ga
1.43 +0.05 -0.05 Ga
c
Craters: 1642
1
D≥100 m
-60 -40 -20 0 20 40 60
km
Craters: 831
2
D≥100 m
50
km
Craters: 1428
3
D≥50 m
-20 0 20
km
4, area=1.20x10³ km²
29 craters, N(1)=9.85x10⁻³ km⁻²
242 craters, N(1)=1.26x10⁻³ km⁻²
809 craters, N(1)=3.83x10⁻⁴ km⁻²
655 +20 -20 Ma
2.15 +0.13 -0.13 Ga
3.76 +0.03 -0.04 Ga
d
5, area=2.40x10³ km²
14 craters, N(1)=5.39x10⁻³ km⁻²
592 craters, N(1)=1.34x10⁻³ km⁻²
887 craters, N(1)=2.79x10⁻⁴ km⁻²
2.29 +0.09 -0.09 Ga
477 12 Ma
3.63 +0.05 -0.08 Ga
e
6, area=8.98x10³ km²
117 craters, N(1)=1.07x10⁻³ km⁻²
778 craters, N(1)=4.24x10⁻⁴ km⁻²
726 +24 -24 Ma
1.83 +0.17 -0.17 Ga
f
Craters: 1128
4
D≥100 m
-60 -40 -20 0 20 40 60
km
Craters: 1639
5
D≥100 m
-50 0 50
km
Craters: 1836
6
D≥100 m
-100 -50 0 50 100
km

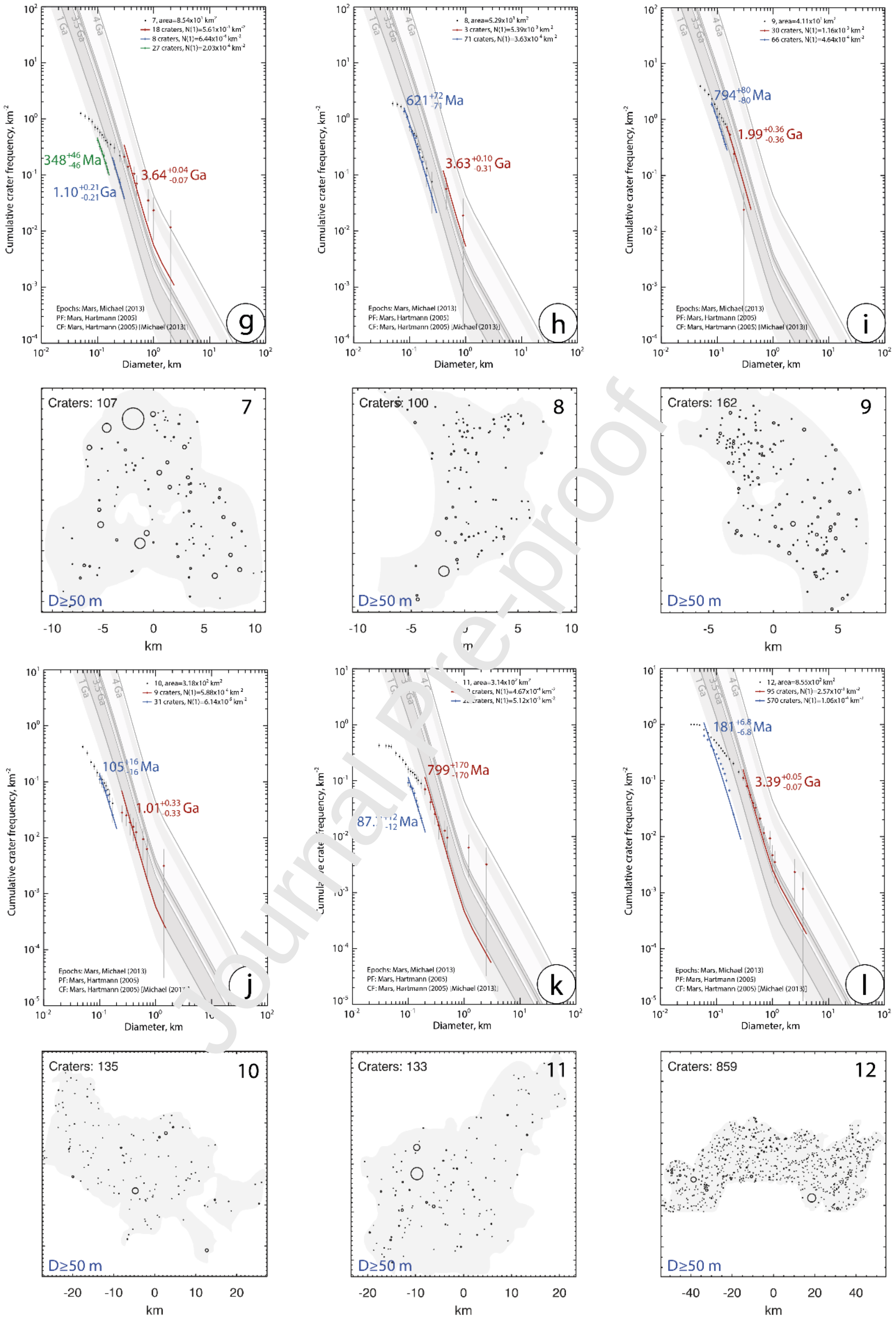

Fig. 8. (a-l) Cumulative crater size-frequency diagrams constructed for estimating the age of the main surface units (above) and corresponding crater-counting areas from 1 to 12 (below) (see locations in Fig. 2b). Age models show simple cumulative fits for the

formation ages (red fit lines) and corrected cumulative fits for the resurfacing events (blue and green fit lines). The grey shadow bands denote the time boundaries between Martian geological epochs according to Michael (2013). “D” and “Craters” refer to the minimum crater diameter and the number of counted craters considered for each counting area, respectively.

km^2, with average age estimates of 1.01 ± 0.33/0.33 Ga (Early to Middle Amazonian) and 0.80 ± 0.17/0.17 Ga (Middle Amazonian), respectively (Fig. 8j, k).

To obtain a minimum age estimate for the cessation of fluvial activity in the main valley of Licus Vallis, we analyzed the crater size-frequency distribution of the crater population developed on the ejecta deposits of the unit AHce$_a$ overlapping the valley. These deposits are related to an impact crater 27 km in diameter formed near the middle course of Licus Vallis, with no evidence of reworking by fluvial activity. The fit for the D >0.3 km crater population provides an estimated age (minimum for fluvial activity) of 3.39 ± 0.05/0.07 Ga (Early to Late Hesperian), considering a counting area of ~860 km^2 (Fig. 8l).

4.4 Subsurface features

To infer possible subsurface structural and stratigraphic features and relationships, we analyzed eight NE-SW-oriented SHARAD ground-penetrating radar profiles acquired across the CNTZ (from west to east: S_01966502, S_02617902, S_01832001, S_02674602, S_02596802, S_01981001, S_01846503, S_02569101). In all these radargrams we have identified potential subsurface radar reflections related to dielectric discontinuities in the subsurface attributable to stratigraphic contacts and fractures with or without shear displacement (e.g., Seu et al., 2007; Castaldo et al., 2017). Here, we illustrate the radargram “S_02596802” because of its representativeness, clarity, and significance, as well as its related simulated cluttergram in order to identify surface echoes (Fig. 9a, b; location in Fig. 2b). The radargram “S_02596802” (Fig. 9a) exhibits, from SW to NE, the following potential subsurface reflective areas indicated by bright sectors (see yellow arrows in Fig. 9a), and numbered from 1 to 5: (1) possible subparallel, closely-spaced returns occurring in deposits of the Cimmeria basin unit ($\mathrm{Nhc_b}$) that fill depressions inset into the Cimmeria dissected unit ($\mathrm{Nhcd_a}$), and are also recognized in the radargram “S_02674602”; (2) possible spatially-dispersed and subparallel reflections reaching a depth of ~3.5 km across the Cimmeria dissected units ($\mathrm{Nhcd_a}$ and $\mathrm{Nhcd_b}$); (3) large detached and downdropped block associated with the dichotomy escarpment with potential backtilted reflections; other large detached blocks (i.e., mesas) with apparently deep fractures (e.g., clefts, gashes) (see Fig. 5a) have been recognized in the radargrams “S_01846503” and “S_01981001”; (4) probable reflections with an overall concave upward geometry, apparently filling a fault-bounded basin ca. 1 km deep with triangular transverse geometry at the foot of the escarpment; and (5) potential discontinuous concave and convex returns up to depths of 1.5 km across the Nepenthes basin and knobby plateau units ($\mathrm{HNtn_b}$ and $\mathrm{Ntn_{kp}}$, respectively), beneath an overall rollover topography sloping toward the escarpment. However, the simulated cluttergram related to “S_02596802” (Fig. 9b) suggests that the potential subsurface returns described in areas (1), (2) and (3) are likely caused by surface echoes, as indicated by red arrows in Fig. 9b.

Steeply dipping discontinuities expressed as dark narrow bands in the radargram “S_02596802” (see white arrows in Fig. 9a) attributable to fractures and faults locally

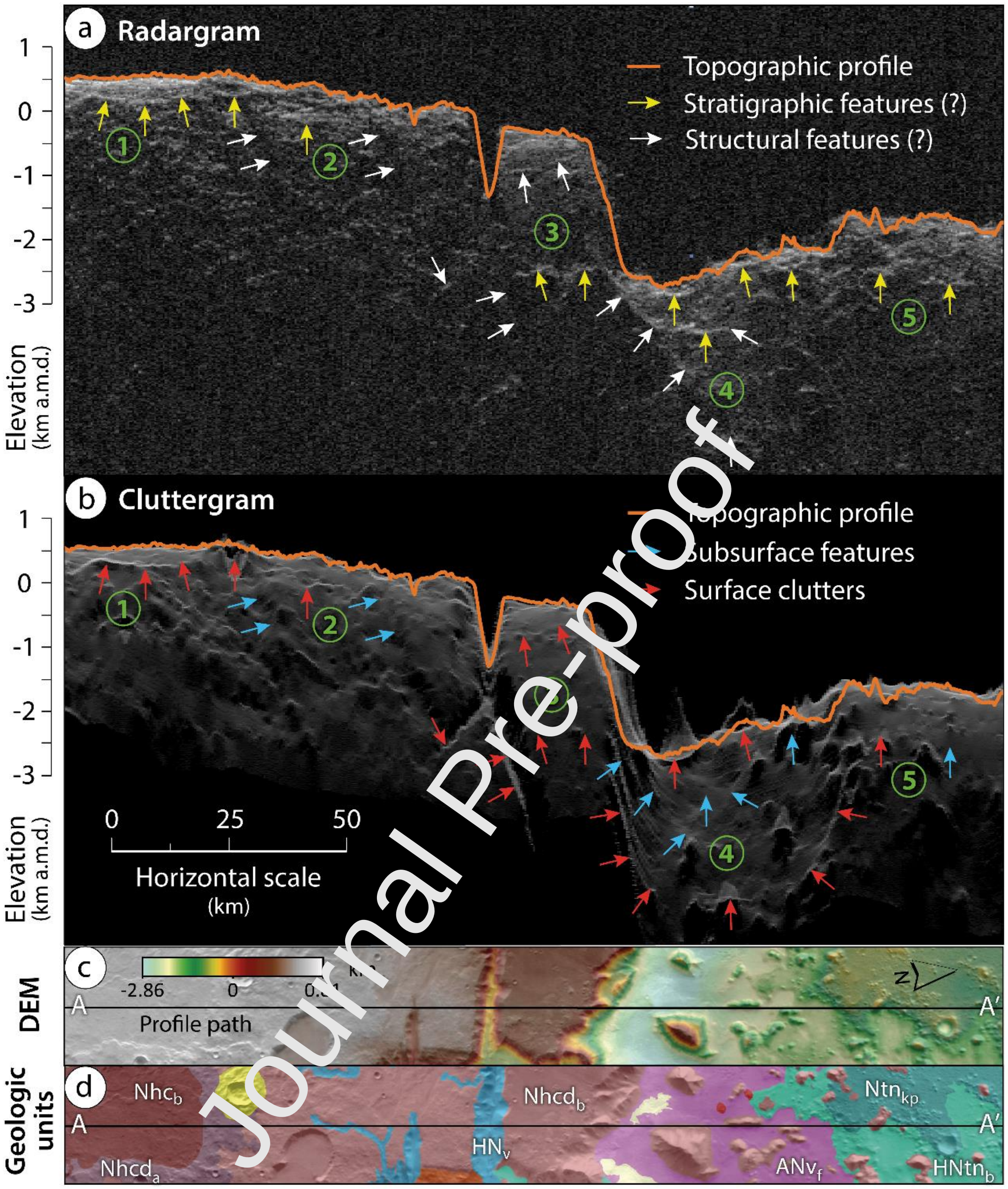

Fig. 9. (a) SHARAD radargram "S_02596802" (see location in Fig. 2b) exhibiting potential subsurface features marked by white and yellow arrows attributable to structural and stratigraphic features, respectively. (b) Simulated cluttergram distinguishing potential subsurface features shown in (a) from surface echoes, as indicated by blue and red arrows, respectively. (c) HRSC/MOLA blended DEM and (d) mapped geologic units, both over a THEMIS-IR day mosaic, showing the topography

and geology of the area around the SHARAD profile, respectively. A-A’ represents the trace of the radargram and that corresponding to the geological cross section shown in Fig. 11.

truncate the potential reflections described above (i.e., stratigraphic contacts). In the Cimmeria region and at the foot of the escarpment these possible fractures and faults dip consistently to the NE and occur associated with down-to-the north topographic drops and troughs. In contrast, the dark, narrow band with a NE dip beneath a significant trough in area (3) is likely caused by surface echoes rather than subsurface returns due to the presence of a large fracture or fault, as shown in Fig. 9b. In the Nepenthes Mensae region they show an antithetic attitude, and together with the discontinuity at the foot of the escarpment mark the lateral boundaries of the sediment-filled basin with triangular section that has been also observed in radargrams “S_02569101”, “S_01981001”, “S_02674602”, “S_01832001”, “S_01966502” and, “S_02617902”.

5. Discussion

The detailed mapping and description of the geology and geomorphology of the CNTZ (Figs. 2-5), together with the spectrally-inferred mineral composition (Figs. 6 and 7), the surface chronology based on both crater-density analysis (Fig. 8) and spatial relationships, and the stratigraphic and structural features interpreted in the radar-sounding data (Fig. 9), have permitted us to: (1) interpret the mapped units and landforms focusing on their formative processes; (2) establish their stratigraphy and correlate them with those of previous geological maps; and (3) propose hypotheses about the landscape evolution and geological history of the area.

5.1 Unit interpretation, stratigraphy and correlation

The Cimmeria dissected units (Nhcd$_a$ and Nhcd$_b$) consist of heavily to moderately degraded highland materials, possibly formed by undifferentiated materials related to impact, volcanic, fluvial, and basin-fill processes. The stratigraphically lower unit Nhcd$_a$, Early to Middle Noachian in age (see summarized age chart in Fig. 10), is affected by locally- and regionally distributed compressional tectonic morpho-structures, as indicated by the occurrence of ridge crests with local distribution, and widespread lobate scarps that indicate a prevalent NE-SW shortening direction sub perpendicular to the dichotomy escarpment. Ridge crests and lobate scarps have been interpreted as the geomorphic expression of thrust or reverse faults (e.g., Watters and Robinson, 1999; Watters et al., 2009). The relatively younger unit Nhcd$_b$ (Middle Noachian) (Fig. 10), locally affected by compressional lobate scarps and ridge crests, displays plateaus, mesas, and knobs along the highland-lowland boundary, probably related to crustal extension and large slope movements (see Figs. 11 and 12). This interpretation is supported by (1) possible radar-inferred NE-dipping normal faults in the Cimmeria region and at the foot of the escarpment, that occur associated with down-to-the-northeast topographic drops and troughs along the dichotomy boundary (Fig. 9a, b); and (2) large detached coherent blocks of Cimmeria that match with arcuate scars in the escarpment, attributable to rock spreads. Both units Nhcd$_a$ and Nhcd$_b$ are integrated in the Middle Noachian highland unit (mNh) defined by Tanaka et al. (2014) in the last global-scale geologic map of Mars. Furthermore, we consider that the Cimmeria 1 unit (Nhc$_1$; Early to Middle Noachian) defined by Skinner and Tanaka (2018) in the Nepenthes Planum region, northwest of our

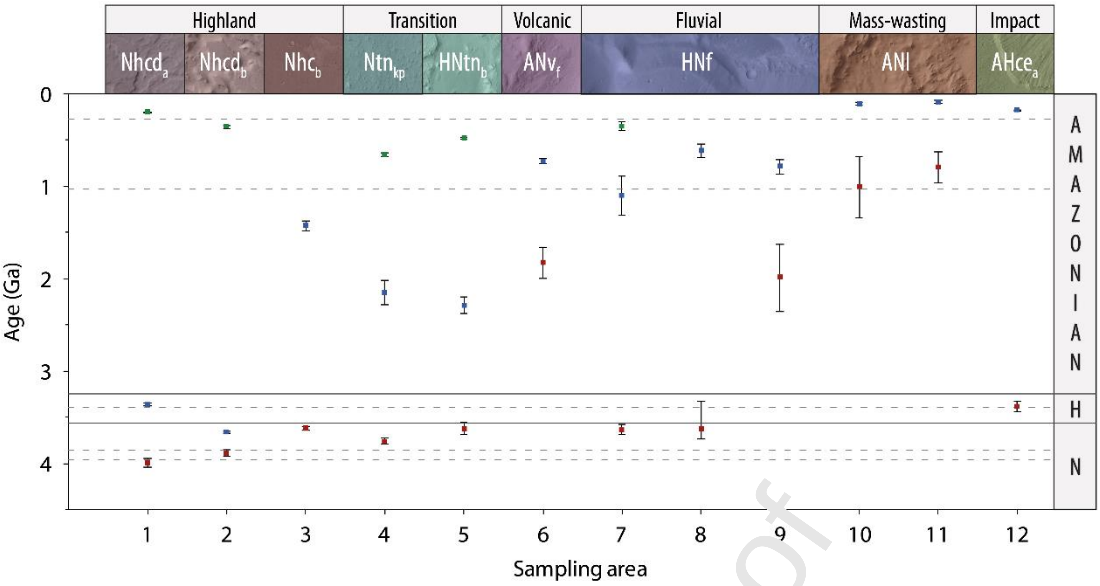

Fig. 10. Diagram showing formation (red boxes) and resurfacing (blue and green boxes) age estimations, as well as their error bars (vertical black lines) obtained for the main mapped units from the cumulative crater size-frequency diagrams constructed for each crater-counting area (Fig. 8) using the Hartmann chronology approach. Horizontal continuous and dashed lines indicate the boundaries between the Martian geological periods and epochs, respectively (Michael, 2013). The top of the diagram shows the geologic unit corresponding to each sampling area. Note that the colors of boxes indicating the ages in this diagram coincide with those shown in Fig. 8. N: Noachian; H: Hesperian.

study area, probably correlates with our unit Nhcd$_b$ due to their similar characteristics, age and topographic occurrence. The division of the Cimmeria region in the CNTZ into two units of different ages was also considered by Scott and Carr (1978) and King (1978) in their global and Mare Tyrrhenum quadrangle geologic maps. They defined for the Cimmeria lower and upper units two Noachian units of hilly and crater material (Nhc), and crater plateau material (Nplc), respectively, characterized by different degree of roughness in their inter-crater surfaces (Scott and Carr, 1978).

The Cimmeria basin unit (Nhc$_b$), Late Noachian in age (Fig. 10), consists of slightly to moderately degraded surfaces, underlain by undifferentiated materials probably corresponding to fluvial sediments and impact breccias that fill depressions inset into unit Nhcd$_a$. These formations are tectonically contracted as indicated by the presence of wrinkle ridges ascribed to thrust faults (e.g., Andrews-Hanna, 2020). This unit probably correlates with the Late Noachian highland unit (lNh) of Tanaka et al. (2014).

The Nepenthes knobby plateau unit (Ntn$_{kp}$; Late Noachian) (Fig. 10) is underlain by deposits including an undifferentiated combination of impact breccias, volcanic products, and mass-wasted materials that form aprons around degraded mesas and knobs of highland rocks of the unit Nhcd$_b$. The unit displays radar-inferred discontinuous layering reaching depths of 1.5 km beneath the downthrown limb of a rollover anticline with topographic expression sloping toward the dichotomy escarpment (Figs. 9a, b and 11). This bending fold suggests a listric geometry for the master normal fault that controls the dichotomy escarpment. The Nepenthes knobby plateau unit shows evidence of compressional tectonics with a dominant NE-SW shortening trend, similar to that exhibited by member a of the Cimmeria dissected unit (Nhcd$_a$), suggesting a common and coetaneous origin for the deformation structures. The unit Ntn$_{kp}$ overlies member b of the Cimmeria dissected unit (Nhcd$_b$), as inferred by the occurrence of relict reliefs (e.g., mesas and knobs) of the unit Nhcd$_b$ that crop out as inliers north of the dichotomy escarpment, and locally underlies the Nepenthes basin unit (HNtn$_b$).

The Nepenthes basin unit (HNtn$_b$; Late Noachian to Early Hesperian), locally showing compressional morpho-structures such as wrinkle ridges, displays pristine to degraded aggradational plains underlain by fluvial, lacustrine and/or mass-wasting deposits. These basins correspond to the belt of interconnected NW-SE-trending closed depressions at the foot of the dichotomy escarpment in Nepenthes Mensae that used to host putative paleolakes (e.g., García-Arnay and Gutiérrez, 2020) (see Fig. 1b). These depressions are inset into member b of the Cimmeria dissected unit (Nhcd$_b$). This unit shows subsurface reflections in the radargrams interpreted as layered deposits with an overall synformal geometry that fill a basin ca. 1 km deep. The basin fill at the foot of the escarpment displays a triangular cross-sectional geometry apparently bounded by synthetic and antithetic normal faults. This structure seems to correspond to a keystone graben associated with the master fault of a larger half-graben morpho-structure with rollover anticline (Figs. 9a, b and 11). In contrast, the basins of the unit HNtn$_b$ located to the northeast of our map are probably the result of the coalescence of degraded impact craters as indicated by their sub-circular shape in plan view, and partially preserved knobby rims (see Fig. 2a). These two mapped units (Ntn$_{kp}$ and HNtn$_b$) were integrated into the Hesperian and Noachian transition unit (HNt) by Tanaka et al. (2014), as well as in the Nepenthes Mensae unit (HNn; Early Noachian to Early Hesperian) defined by Tanaka et al. (2005) in their geologic map of the northern plains of Mars. In the region of Nepenthes Planum, Skinner and Tanaka (2018) defined the Cimmeria 2 unit (Nhc$_2$; Middle to Late Noachian) and Cimmeria 3 unit (HNhc$_3$; Late Noachian to Early Hesperian) that possibly correlate with our mapped units Ntn$_{kp}$ and HNtn$_b$, respectively, as suggest their similar characteristics, stratigraphic position and chronology. Tanaka et al. (1992b) defined in their geologic map of the Elysium region the undivided material unit HNu (Noachian to Early Hesperian) and the smooth-plains material unit Aps (Early Amazonian), that also correlate with our mapped units Ntn$_{kp}$ and HNtn$_b$, respectively. The unit Aps defined by Tanaka et al. (1992b) shows poorly constrained spatial boundaries and chronology, with a remarkable younger age than the age estimations obtained for those surfaces by Skinner and Tanaka (2018) and in this work.

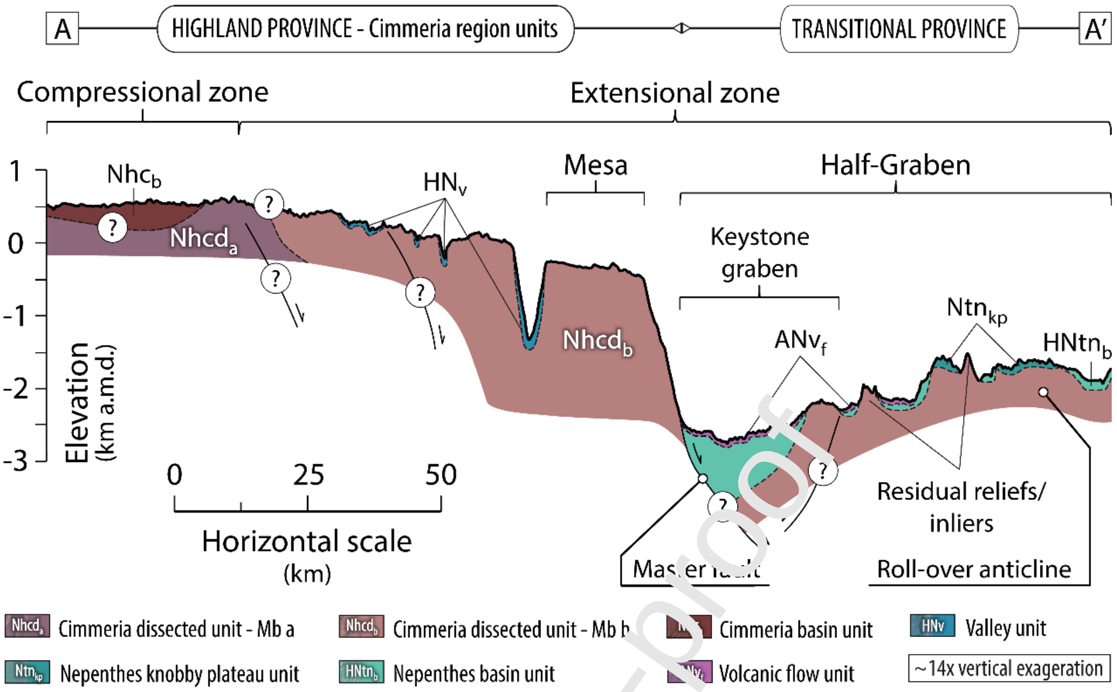

Fig. 11. Geological cross-section A-A' (see location in Fig. 2b) illustrating our interpretation of the subsurface stratigraphic and structural relationships in the CNTZ. This schematic cross-section has been constructed based on the information provided by the radargram profile "S_02596802" shown in Fig. 9, topographic and chronological data, as well as cross-cutting and superposition relationships among geologic units. Colors coincide with those of the geologic units shown in Fig. 2a.

The fan unit (HNf), Late Noachian to Late Hesperian in age (Fig. 10), corresponds to the fan-shaped deposits interpreted as putative Gilbert-type deltas and alluvial fans (e.g., Rivera-Hernández and Palucis, 2019; García-Arnay and Gutiérrez, 2020). These water-laid deposits show spectrally inferred hydrated clay- and silica-bearing layered sediments (Figs. 6 and 7) in the putative deltas "D2" and "D11" (see Table 1). The spectra of the hydrated Fe/Mg-phyllosilicates and hydrated Al-phyllosilicates/silica are, respectively, consistent with an intermediate composition between endmember smectites saponite and nontronite, and between opal and the endmember smectite montmorillonite (Fig. 6c, d). The detection of hydrated minerals together with the morpho-sedimentary environment supports the presence of liquid water in the past (e.g., Poulet et al., 2005). Their high paleoenvironmental interest is also related to the relatively rapid aggradation rate that characterizes these sedimentary environments, favoring the preservation of potentially existing organic matter (e.g., Ehlmann et al., 2008; Summons et al., 2011).

To estimate the chronology of this unit, we selected the two largest putative deltas in the CNTZ (i.e., “D2” and “D7”, Table 1). The areas of these fan-shaped deposits (<100 km^2) are significantly smaller than 1,000 km^2, which is the minimum threshold area for confidently assessing the age of a surface according to Warner et al. (2015). This implies that age estimations obtained for these surfaces may be affected to a greater extent by the spatial variability of cratering processes, as well as the exclusion of larger craters resulting in lower crater counts (i.e., potential age underestimation). We obtained a surface age of 1.99 ± 0.36/0.36 Ga (Early Amazonian) for the upper fan of “D2”, that represents the smaller putative delta area (~41.1 km^2). The upper fan partially overlies the lower fan of “D2” suggesting that the former is younger. In fact, its formation age is significantly younger than that estimated for the lower fan of “D2” (3.63 ± 0.10/0.31 Ga; Late Noachian to Late Hesperian). In contrast, the age estimated for the lower fan of “D2” is consistent with that estimated for the putative delta “D7” (3.64 ± 0.04/0.07 Ga; Late Noachian). Both ages agree with the period of intense and widespread fluvial activity on Mars (e.g., Irwin III et al., 2005; Carr, 2012), and also fit with that estimated for the Nepenthes basin unit (HNtn$_b$) (3.63 ± 0.05/0.08 Ga; Late Noachian to Early Hesperian), probably filled by coeval deposits related to fluvial and lacustrine processes.

Additionally, we obtained a minimum age estimate of 3.39 ± 0.05/0.07 Ga (Early to Late Hesperian) (Fig. 10) for the cessation of fluvial activity in Licus Vallis, the main watershed in the CNTZ. This age estimation is also compatible with the older ages obtained for the putative deltas “D7” and “D2” (lower fan), and the Nepenthes basin unit ($HNtn_b$). Based on these results, we assigned an age of Late Noachian to Late Hesperian to the valley unit (HNv).

García-Arnay and Gutiérrez (2020) obtained a formation age of 3.88 ± 0.06/0.12 Ga (Middle Noachian to Late Noachian) for the putative delta “D7”, using the same approach as the one applied in the present work (the Hartmann chronology), but without establishing a minimum crater diameter (i.e., all primary craters observed were counted). The formation age obtained by García-Arnay and Gutiérrez (2020) is older than that estimated in this work (3.64 ± 0.04/0.07 Ga; Late Noachian). The difference between the closest extremes of the 1-sigma standard deviation error bars for each formation age is only 80 Ma (3.76 vs 3.68 Ga, respectively). We interpret that this non-significant age difference is mainly due to exclusion in this work of the craters with diameters lower than the considered threshold value (50 m), as well as the inclusion of the putative delta front (larger counting area) potentially affected by erosion and slope instability processes (resurfacing).

In summary, the chronological analysis indicates that (1) fluvial-lacustrine processes mainly occurred in the CNTZ from Late Noachian to Late Hesperian; (2) the higher impact of the spatial variability of cratering processes in smaller areas, as well as the minimum crater diameter considered in the computation (50 m) may have led to underestimated ages for the putative deltas; and (3) the formation age obtained for the upper fan of “D2”, which overlies the lower fan (e.g., de Pablo and Pacifici, 2008), does not seem to be consistent with a period of intense fluvial activity during the Early

Amazonian (~2 Ga), but seems to be related to the small size of the analyzed area and possible resurfacing events affecting its crater population.

The volcanic flow unit (ANv_f) consists of high-TI plains most probably formed by lava fields, as indicated by the following lines of evidence: (1) frequent grooves and channels, as well as overlapping lobes often emanating from isolated and coalesced raised fissures, pitted cones and small tholi of the unit ANv_e, interpreted as different types of volcanic edifices genetically linked to the unit ANv_f, and thus, with an analogous age (see Fig. 3b and h-k); (2) extensive olivine-bearing deposits associated with barchan dune fields (unit Ae) that occur along the southern edges of the unit ANv_f (see Figs. 3l and 7); and (3) it generally occurs in the deepest areas of the depressions likely related to subsidence processes within an extensional tectonic environment (Figs. 11 and 13). The localized deformation of this unit by wrinkle ridges is probably associated with thermal contraction of cooling lava flows. We obtained for the volcanic flow unit an age estimate of 1.83 ± 0.17/0.17 Ga (Early Amazonian) (Fig. 10). However, we have corrected its formation age based on more robust relative chronologies based on geometrical relationships (e.g., cross-cutting and superposition). The deposits corresponding to the lower fan of “D2” (unit HNf; Late Noachian to Late Hesperian) locally overlie the volcanic flow and volcanic edifice units (see details in Fig. 3j). We thus consider that the minimum age for the formation of the volcanic flow unit should be at least as old as that of the unit HNf (i.e., Late Noachian). The relatively young formation age obtained by crater counting for the unit ANv_f may be attributed to the obliteration of old craters because of the eolian erosion and/or locally younger volcanic activity. García-Arnay and Gutiérrez (2020) obtained a surface age of 3.71 ± 0.08/0.21 Ga (Late Noachian to Early Hesperian) for the low-lying terrains located east of the counting area “6” applying the same dating approach (i.e., the Hartmann chronology), but without considering any minimum crater diameter. This age fits with our minimum age estimate for the formation of the volcanic flow unit (Late Noachian). However, the counting area considered by García-Arnay and Gutiérrez (2020) also included zones corresponding to other geologic units and, as a result, the obtained age is not a reliable estimate for the volcanic flow unit.

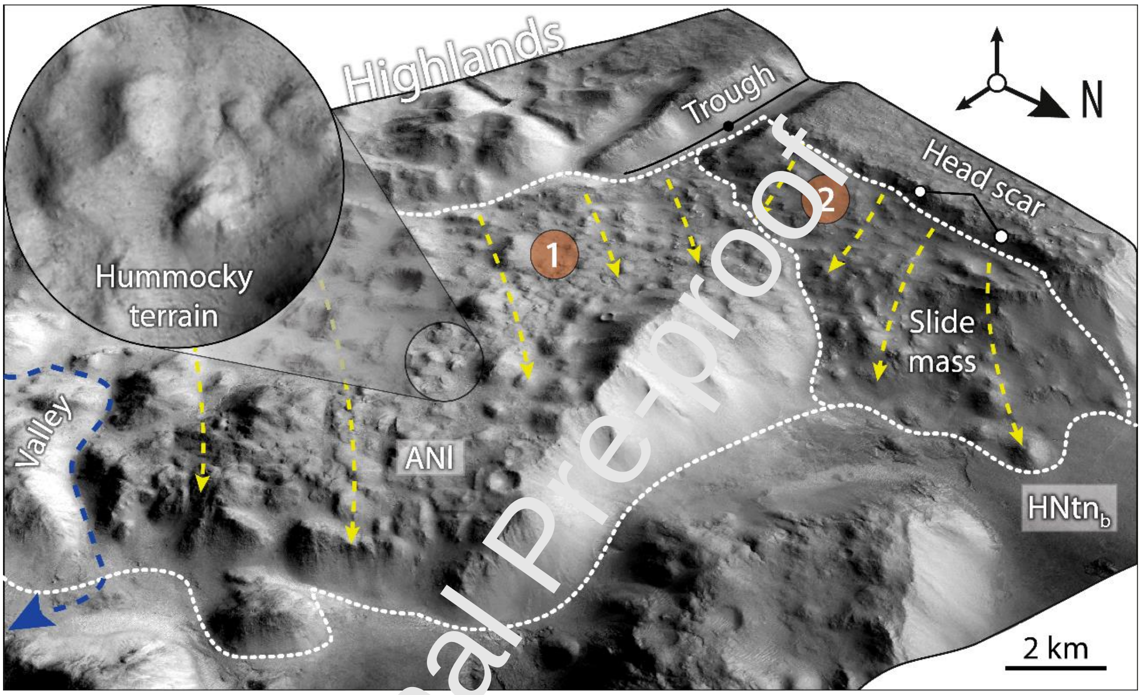

Fig. 12. 3D oblique view of two large landslides (ANl unit) occurring along the dichotomy escarpment in the CNTZ (location in Fig. 1a; CTX images). The landslide 2 located on the right side to the image (labelled as "2") seems to overlap the larger landslide 1. Note the presence of hummocky topography on the landslide surfaces (circle: close-up view; CTX images). Landslide 1 is incised by a valley of the unit HNv. White dashed line indicates the toe of the landslide mass overriding the surrounding plains of the Nepenthes basin unit (HNtn$_b$). Blue and yellow dashed arrows indicate the paleoflow of the valley and the displacement direction of the landslides, respectively. The landslide of this 3D image corresponds with the counting area 10 (Figs. 8j and 10).

The unit ANv$_f$ in the CNTZ is integrated into the Hesperian and Noachian transition unit (HNt) of Tanaka et al. (2014) and does not seem to be correlative to the Nepenthes flow unit (Htn_f) of the Nepenthes Planum region (Skinner and Tanaka, 2018).

The landslide unit (ANl) consists of mass-wasted highland materials derived from the dichotomy escarpment formed by unit $Nhcd_b$ and locally accumulated along the slopes of the dichotomy escarpment during the Late Noachian to Middle Amazonian. We have interpreted this unit as deposits of various types of large landslides based on the following features: (1) the presence of head scars that match with large, detached blocks, backtilted benches, as well as rugged, rolling, and hummocky surfaces locally with blocky texture; (2) their spatial association with the ca. 2 km high dichotomy escarpment; and (3) the extensional environmental that dominates the basins adjacent to the dichotomy. These large landslides, which occur along the dichotomy escarpment and have moved into the depressions in Nepenthes Mensae, are generally characterized by a limited runout. We have inferred different types of slope movements in the CNTZ based on the classification of Hungr et al. (2014): (1) detached, km-scale masses of coherent blocks, locally fractured and dilated, probably formed by lateral spreading related to weak basal materials (see an example in Fig. 5a), (2) deposits characterized by apparent internal deformation, slump blocks and often back-tilted benches possibly formed by rotational sliding (e.g., landslides 1 and 2 in Fig. 12), as well as (3) frequent rock falls. We obtained average age estimates of 1.01 ± 0.33/0.33 Ga (Early to Middle Amazonian) and 0.80 ± 0.17/0.17 Ga (Middle Amazonian) for each counting area considered (Fig. 10). However, the occurrence of a valley originating in the highlands (unit HNv; Late Noachian to Late Hesperian) and dissecting the landslide deposits (see Fig. 12) indicates that the minimum age estimation for the formation of the unit ANl may be as old as Late Noachian.

As previously stated, the confidence in age estimates obtained for the counting areas smaller than 1,000 km^2 (i.e., counting areas 3 and from 7 to 12; see Fig. 10) may have been affected by probable variations in cratering and potential age underestimation (Warner et al., 2015). Although these estimates should be treated with caution there is an overall consistency between the model ages and the relative ages indicated by the stratigraphic and geomorphic relationships.

5.2 Geological-geomorphological history of the CNTZ

Here, we summarize the geological history and landscape evolution of the CNTZ inferred based on the interpretation of the mapped units and landforms and their chronology. Our reconstruction is focused on the sequence of paleogeographic stages associated with the formation of the closed depressions that used to host large paleolakes and on the evolution of the dichotomy escarpment.

The explored record starts in the Early to Middle Noachian with the formation of the Cimmeria dissected units (the lower and upper members Nhcd$_a$ and Nhcd$_b$, respectively). Both units were affected by a phase of NE-SW-oriented tectonic shortening, recorded by prominent lobate scarps interpreted as the surface expression of thrust faults. These morpho-structures occur in the highland province (e.g., Watters and Robinson, 1999; Watters, 2003b), and less conspicuously in the Nepenthes knobby plateau unit (Ntn$_{kp}$, Late Noachian in age) of the transitional province. The disruption of fluvial valleys (Late Noachian to Late Hesperian in age) observed in the unit Nhcd$_a$ by lobate scarps unaffected by fluvial erosion, as well as the adaptation of some drainages to these compressional features (e.g., deflected fluvial valleys parallel to the toe of lobate scarps) suggest that the compressional stress field may have started as soon as the Late Noachian and probably ended sometime after the cessation of fluvial activity (Late

Hesperian), which is roughly consistent with the global-scale compressional tectonic regime that occurred on Mars between the Late Noachian to Early Hesperian (e.g., Tanaka et al., 1991; Watters, 1993). During the Late Noachian, basins of uncertain origin were formed and filled of sediments on the unit Nhcd$_a$ to form the Cimmeria basin unit (Nhc$_b$) (see Fig. 11).

The topography of the Cimmeria dissected units in the CNTZ is analogous to that displayed in a large part of the highlands south of the dichotomy, which is characterized by a topographically higher sector that gradually descends from the highlands into the northern lowlands and frequently ends abruptly along a steep escarpment that represents the dichotomy boundary (Watters and McGovern, 2006). The ca. 2 km high escarpment in the CNTZ defines the boundary between the highland and transitional provinces. The member b of the Cimmeria dissected units (Nhcd$_b$) associated with the dichotomy escarpment shows numerous troughs that controlled fretted valleys subparallel to the escarpment. The analyzed radargrams indicate that the escarpment and the troughs are probably related to a master and secondary normal faults that dip consistently to the NE indicating a NE-SW extension direction with major geomorphic imprint on the landscape (see Figs. 9 and 11). The extensional tectonics probably led to: (1) the plateau situated south of the dichotomy escarpment with down-to-the-north topographic drops associated with secondary normal faults; and (2) the chain of interconnected NW-SE-trending closed depressions located at the foot of the dichotomy escarpment. These basins are probably downthrown blocks (i.e., keystone graben) nested in the lower part of a larger half-graben morpho-structure (i.e., fault-angle depression), as inferred from the topography and the stratigraphic and structural relationships interpreted from the mapped units and radar reflections (see Figs. 9 and 11).

According to Tanaka et al. (2005), the region of Nepenthes Mensae may have been affected by mass wasting and “basal sapping of volatiles” that may have generated the knobby terrain in this region. The belt of depressions in Nepenthes Mensae was also attributed to extensional tectonics by Watters (2003a) and Watters and McGovern (2006), reaching the maximum lithospheric deflection near the base of the dichotomy escarpment (Watters, 2003a). Other graben basins have been inferred along the crustal dichotomy in Nilosyrtis Mensae (Levy et al., 2007) and Protonilus Mensae (e.g., Watters, 2003a), located north of Terra Sabaea and Arabia Terra, respectively, as well as in Aeolis Mensae (e.g., Watters and McGovern, 2006), southeast of the CNTZ, exhibiting a topographic expression analogous to that in the study area. Our observations also suggest that, regardless of how and when the crustal dichotomy was formed, its current shape in the CNTZ is largely related to dip-slip displacement along a down-to-the-northeast normal fault system that controlled the formation of half-graben basins within this extensional environment in Nepenthes Mensae (see Figs. 11 and 13). The Nepenthes basin unit (HNtn$_b$), which is generally confined to the lower part of the half-graben basins (nested keystone graben) and seems to reach its greatest thickness in the vicinity of the fault-controlled escarpment (see Figs. 11 and 13), was accumulated from the Late Noachian to Early Hesperian based on crater densities. The probable syntectonic deposition of the unit HNtn$_b$ by fluvio-lacustrine and mass-wasting processes suggests that extensional tectonics in the CNTZ was active at least during the Late Noachian to Early Hesperian. The volcanic edifice/flow units (ANv$_e$ and ANv$_f$, respectively), probably associated with extensional tectonics (i.e., fissure eruptions), were locally emplaced overlying the unit HNtn$_b$ from the Late Noachian to the Early Amazonian, as indicated by crater densities and geometrical relationships among units (see the block diagram in Fig. 13), what suggests that the extensional phase may have even been active until Early Amazonian times. The stratigraphic relationships between the volcanic units (ANv$_e$ and ANv$_f$) and the fan unit (HNf; Late Noachian to Late Hesperian), which is rich in clay-bearing deposits (Figs. 6 and 7), reveal that the latter at least locally postdated the volcanic units (see an example in Fig. 13). However, their ages based on both crater densities and

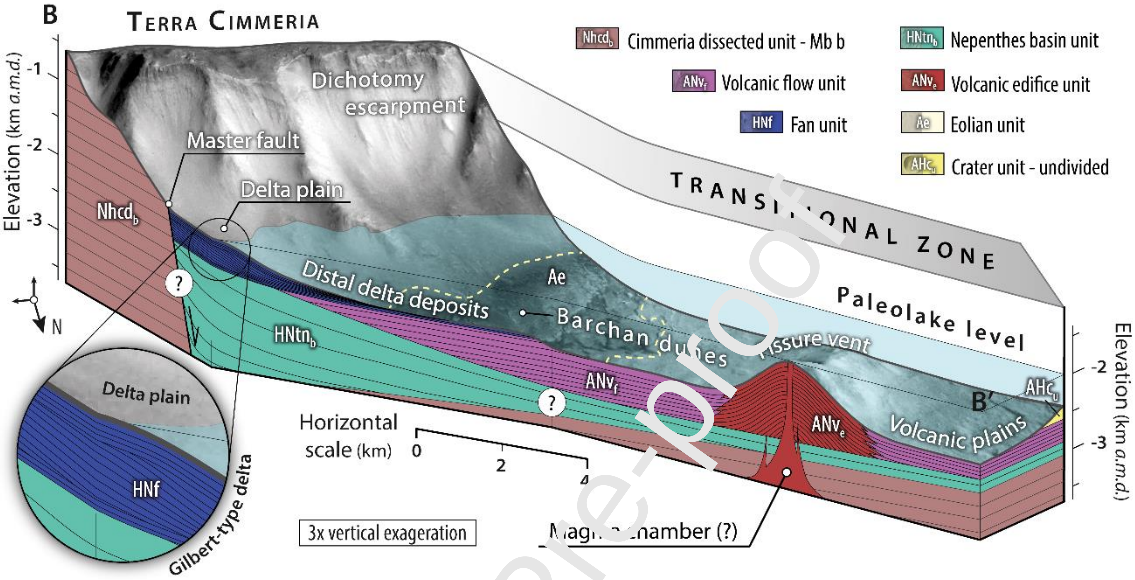

Fig. 13. Detailed block diagram showing a tectono-sedimentary model of the CNTZ around the dichotomy escarpment that interprets the subsurface geology along the cross section B-B' (location and details in Figs. 2b and 7a, respectively) integrating the information provided by topographic data, the geologic units, radargrams, formation ages and mineral composition of the units. It includes the reconstruction of the paleolake level at about -1950 m, which is the mean water level of the main paleolake in Nepenthes Mensae during the Late Noachian-Early Hesperian transition according to García-Arnay and Gutiérrez (2020). Colors coincide with those of the geologic units shown in Fig. 2a. Circle: close-up view showing the interpreted depositional architecture of the putative Gilbert-type delta "D11" (see Table 1).

stratigraphic relationships suggest that the volcanic and the fluvio-lacustrine activity may have been at least partially coeval, between the Late Noachian and the Late

Hesperian, coinciding with the period of fluvial activity and formation of paleolakes in the CNTZ (Fig. 13) (e.g., Rivera-Hernández and Palucis, 2019; García-Arnay and Gutiérrez, 2020).

Our observations indicate that the inferred compressional and extensional tectonic stresses in the CNTZ, which exhibit the same direction (i.e., NE-SW), seem to have largely occurred sometime from the Late Noachian to Late Hesperian, and even until more recent epochs, but not simultaneously. Several lines of evidence suggest that the extensional phase postdated the compressional deformation: (1) the compressional structures do not affect to the most recent units; (2) the extensional structures have formed the most recent morpho-structures (e.g., the present-day dichotomy escarpment or the basins in Nepenthes Mensae), as well as the accommodation space in which the units $HNtn_b$ and ANv_f were deposited; and (3) the areas affected by extensional tectonics divide in half those that are tectonically contracted in the highland and transitional provinces. Other authors (e.g., McGill and Dimitriou, 1990; Watters and Robinson, 1999; Watters, 2003a, 2003b) indicated that the compressional and extensional deformation occurred along the dichotomy boundary in the Eastern Hemisphere from the Late Noachian to Early Hesperian. Different types of large landslides have been developed along the dichotomy escarpment favored by the large local relief, and probably also by its continuous tectonic rejuvenation and the weakening of the materials by extensional deformation (i.e., faulting, fracturing). Basal sapping suggested by Tanaka et al. (2005) may have contributed to the instability and development of the escarpment in Nepenthes Mensae. A tentative Late Noachian to Middle Amazonian age has been ascribed to the landslide unit (ANl) based on crater densities and stratigraphic relationships, although the different slope movements may have a wide range of chronologies. The presence of mechanically weak material in the basal part of the escarpment may have propitiated the development of large rock spreads, producing coherent blocks with dilated fractures of unit Nhcd$_b$ detached form the escarpment and displaced laterally into the depressions of Nepenthes Mensae (see an example of large rock spreads located ~15 km away from the dichotomy escarpment in Fig. 5a). During the Amazonian period, significant eolian erosion has mainly carved the surfaces of the knobby plateau and basin units in Nepenthes Mensae, as shown by the pervasive occurrence of yardangs that indicate a dominant SE-directed wind (see Fig. 3a). Numerous barchan dune fields formed by olivine-bearing sands (Fig. 7) have been accumulated along the foot of the dichotomy escarpment in recent times (see Figs. 3l and 13).

6. Conclusions

The findings suggest that the exposed units mapped in the CNTZ formed over a long time-span, from the Early Noachian to recent times. The inferred compressional and extensional deformation have played a fundamental morphogenetic role in the configuration of the landscape at least from the Late Noachian to Late Hesperian. Extensional tectonics, which postdates the compressional phase, has contributed to the development of some of the most prominent geomorphic features of the region, including: (1) the plateau located to the south of the dichotomy in the highland province; (2) the 2-km-high dichotomy escarpment interpreted as a fault scarp related to the master normal fault (3) the formation of a half-graben at the foot of the escarpment with keystone grabens nested in its lower part that used to host paleolakes in Nepenthes Mensae; (4) the fissure-type volcanic activity in the deepest areas of the basins; and (5) the mega landslides (e.g., large rock spreads and slumps) derived from the dichotomy escarpment. Fluvial and lacustrine activity has also played an important morphogenetic role in the CNTZ. This interpretation is supported by the pervasive occurrence of tectonically-controlled fluvial valley networks carved into the Cimmeria dissected units, and putative fan-deltas, rich in hydrated clay-bearing layered sediments. The possible interaction during the Late Noachian to Late Hesperian between the heat sources associated with the volcanic activity and the liquid water occupying the basins in Nepenthes Mensae makes this region a potential landing site for the search of past life signatures on Mars. This work contributes to improve our knowledge about the geology and the landscape evolution in the CNTZ, and provides a detailed geologic framework to contextualize the recent findings about the paleohydrologic conditions in Nepenthes Mensae, as well as to compare future studies within the CNTZ and other areas along the highland-lowland transitional zone.

Acknowledgments

This research was supported by a PhD scholarship granted to ÁG-A (C237/2016) by the Gobierno de Aragón (Spain) and the European Social Fund, as well as by grants awarded by the Ibercaja-CAI mobility programme (CB 2/21; Universidad de Zaragoza, Fundación Bancaria Ibercaja and Fundación CAI) and the Erasmus+ Traineeship programme (53971; European Commission) to fund a three-month research stay of ÁG-A at the International Research School of Planetary Sciences (IRSPS, Università degli Studi "G. D'Annunzio"). The work has been also supported by projects CGL2017-85045-P and PID2021-123189NB-I00 (Ministerio de Ciencia e Innovación, Gobierno de España). We would like to express our gratitude to Dr. Gian Gabriele Ori and Dr. Andrea Pacifici for their hospitality and support during the research stay of Á.G-A at the IRSPS. We would also like to thank Dr. Tim Goudge and an anonymous reviewer, as well as the editor, Dr. Martin Stokes, for their valuable suggestions and comments, which helped to improve this paper.

References

Andrews-Hanna, J.C., 2020. The tectonic architecture of wrinkle ridges on Mars. Icarus 351, 113937. https://doi.org/10.1016/j.icarus.2020.113937.

Andrews-Hanna, J.C., Zuber, M.T., Banerdt, W.B., 2008. The Borealis basin and the origin of the martian crustal dichotomy. Nature 453(7199), 1212-1215. https://doi.org/10.1038/nature07011.

Brown, A.J., Calvin, W.M., McGuire, P.C., Murchie, S.L., 2010. Compact Reconnaissance Imaging Spectrometer for Mars (CRISM) south polar mapping: First Mars year of observations. Journal of Geophysical Research: Planets, 115(E2). https://doi.org/10.1029/2009JE003333.

Burr, D.M., Williams, R.M., Wendell, K.D., Chojnacki, M., Emery, J.P., 2010. Inverted fluvial features in the Aeolis/Zephyria Plana region, Mars: Formation mechanism and initial paleodischarge estimates. J. Geophys. Res. Planets 115(E7). https://doi.org/10.1029/2009JE003496.

Carr, M.H., 2012. The fluvial history of Mars. Phil. Trans. R. Soc. A. 370(1966), 2193-2215. https://doi.org/10.1098/rsta.2011.0500.

Carter, J., Poulet, F., Bibring, J.-P., Mangold, N., Murchie, S., 2013. Hydrous minerals on Mars as seen by the CRISM and OMEGA imaging spectrometers: updated global view. J. Geophys. Res. Planets 118, 831–858. https://doi.org/10.1029/2012JE004145.

Castaldo, L., Mège, D., Gurgurewicz, J., Orosei, R., Alberti, G., 2017. Global permittivity mapping of the Martian surface from SHARAD. Earth Planet. Sc. Lett. 462, 55-65. https://doi.org/10.1016/j.epsl.2017.01.012.

Choudhary, P., Holt, J.W., Kempf, S.D. 2016. Surface clutter and echo location analysis for the interpretation of SHARAD data from Mars. IEEE Geoscience and Remote Sensing Letters, 13(9), 1285-1289. https://doi.org/10.1109/LGRS.2016.2581799.

Christensen, P.R., Jakosky, B.M., Kieffer, H.H., Malin, M.C., McSween, H.Y., Nealson, K., Mehall, G.L., Silverman, S.H., Ferry, S., Caplinger, M., Ravine, M., 2004. The thermal emission imaging system (THEMIS) for the Mars 2001 Odyssey Mission. Space Sci. Rev. 110 (1–2), 85–130. https://doi.org/10.1023/B:SPAC.0000021008.16305.94.

Christensen, P.R., Fergason, R.L., Edwards, C.S., Hill, J., 2013. THEMIS-derived thermal inertia mosaic of Mars: product description and science results. Lunar and Planetary Science Conference Abstracts vol. 44 (p. #2822).

Clarke, J., Pain, C.F., Rupert, S., 2020. Complex expressions of inverted and exhumed relief in central Utah, and some martian counterparts. Phys. Geogr. 1-18. https://doi.org/10.1080/02723646.2020.1839161.

Cull, S., Arvidson, R.E., Morris, R.V., Wolff, M., Mellon, M.T., Lemmon, M.T., 2010. Seasonal ice cycle at the Mars Phoenix landing site: 2. Postlanding CRISM and ground observations. Journal of Geophysical Research: Planets, 115(E5). https://doi.org/10.1029/2009JE003340.

de Pablo, M.Á., Pacifici, A., 2008. Geomorphological evidence of water level changes in Nepenthes Mensae, Mars. Icarus 196 (2), 667–671. https://doi.org/10.1016/j.icarus.2008.04.005.

Di Achille, G., Hynek, B.M., 2010. Ancient ocean on Mars supported by global distribution of deltas and valleys. Nat. Geosci. 3 (7), 459–463.

https://doi.org/10.1038/ngeo891.

Dickson, J.L., Kerber, L.A., Fassett, C.I., Ehlmann, B.L., 2018. A global, blended CTX mosaic of Mars with vectorized seam mapping: a new mosaicking pipeline using principles of non-destructive image editing. Lunar and Planetary Science Conference Abstracts vol. 49 (p. #2480).

Dickson, J.L., Lamb, M.P., Williams, R.M.E., Hayden, A.T., Fischer, W.W., 2021. The global distribution of depositional rivers on early Mars. Geology, 49(5), 504-509. https://doi.org/10.1130/G48457.1.

Edwards, C.S., Nowicki, K.J., Christensen, P.R., Hill, J., Gorelick, N., Murray, K., 2011. Mosaicking of global planetary image datasets: 1. Techniques and data processing for Thermal Emission Imaging System (THEMIS) multi- spectral data. Journal of Geophysical Research: Planets, 116(E10). https://doi.org/10.1029/2010JE003755.

Ehlmann, B.L., Mustard, J.F., Fassett, C.I., Schon, S.C., Head III, J.W., Des Marais, D.J., Grant, J.A., Murchie, S.L., 2008. Clay minerals in delta deposits and organic preservation potential on Mars. Nat. Geosci. 1 (6), 355–358. https://doi.org/10.1038/ngeo207.

Ehlmann, B.L., Mustard, J.F., Swayze, G.A., Clark, R.N., Bishop, J.L., Poulet, F., Des Marais, D.J., Roach, L.H., Milliken, R.E., Wray, J.J., Barnouin-Jha, O.S., Murchie, S.L., 2009. Identification of hydrated silicate minerals on Mars using MRO-CRISM: geologic context near Nili Fossae and implications for aqueous alteration. J. Geophys. Res. Planets 114, E2. https://doi.org/10.1029/2009JE003339.

Elkins- Tanton, L.T., Hess, P.C., Parmentier, E.M., 2005. Possible formation of ancient crust on Mars through magma ocean processes. J. Geophys. Res. Planets 110(E12). https://doi.org/10.1029/2005JE002480.

Fergason, R.L., Christensen, P.R., Kieffer, H.H., 2006. High- resolution thermal inertia derived from the Thermal Emission Imaging System (THEMIS): Thermal model and applications. J. Geophys. Res. Planets 111(E12). https://doi.org/10.1029/2006JE002735.

Fergason, R.L., Hare, T.M., Laura, J., 2018. HRSC and MOLA Blended Digital Elevation Model at 200m v2, Astrogeology PDS Annex. U.S. Geological Survey http://bit.ly/HRSC_MOLA_Blend_v0.

Frey, H., Shultz, R.A., 1988. Large impact basins and the mega-impact origin for the crustal dichotomy on Mars. Geophys. Res. Lett. 15, 229–232. https://doi.org/10.1029/GL015i003p00229.

Frey, H.V., Schultz, R.A., Maxwell, T.A., 1986. The Martian crustal dichotomy: Product of accretion and not a specific event? Lunar and Planetary Science Conference Abstracts vol. 17, pp. 241-242.

García-Arnay, Á., Gutiérrez, F., de Pablo, M.Á., Fernández, S., 2018a. Characterization and interpretation of the fan-shaped and terrace-like features identified in Nepenthes Mensae, Mars. EGU General Assembly Conference Abstracts vol. 20 (p. # 808). Retrieved from: https://figshare.com/articles/Characterization_and_interpretation_of_the_fanshaped_and_terrace-like_features_identified_in_Nepenthes_Mensae_Mars/9824609.

García-Arnay, Á., Fernández, S., de Pablo, M.Á., Gutiérrez, F., 2018b. The dominant morphogenetic role of surface runoff in Licus Vallis, Mars: results from geomorphological and morphometric analyses. Geogaceta 63, 63–66 Retrieved from: http://www.sociedadgeologica.es/archivos/geogacetas/geo63/geo63_16.pdf.

García-Arnay, Á., Gutiérrez, F., 2020. Reconstructing paleolakes in Nepenthes Mensae, Mars, using the distribution of putative deltas, coastal-like features, and terrestrial analogs. Geomorphology 359, 107129.

https://doi.org/10.1016/j.geomorph.2020.107129.

Golabek, G.J., Keller, T., Gerya, T.V., Zhu, G., Tackley, P.J., Connolly, J.A., 2011. Origin of the Martian dichotomy and Tharsis from a giant impact causing massive magmatism. Icarus 215(1), 346-357. http://dx.doi.org/10.1016/j.icarus.2011.06.012.

Goudge, T.A., Fassett, C.I., 2018. Incision of Licus Vallis, Mars, from multiple lake overflow floods. J. Geophys. Res. Planets 123 (2), 405–420. https://doi.org/10.1002/2017JE005438.

Greeley, R., Guest, J., 1987. Geologic map of the eastern equatorial region of Mars. U.S. Geological Survey, IMAP 1802, Scale 1:5,000,000. https://doi.org/10.3133/i1802B.

Greeley, R., Batson, R.M., 1990. Planetary Mapping. Cambridge Univ. Press p. 296.

Hansen, V.L., 2000. Geologic mapping of tectonic planets. Earth Planet. Sc. Lett. 176(3–4), 527–542. https://doi.org/10.1016/S0012-821X(00)00017-0.

Hartmann, W.K., 2005. Martian cratering 8: isochron refinement and the chronology of Mars. Icarus 174 (2), 294–320. https://doi.org/10.1016/j.icarus.2004.11.023.

Hayden, A.T., Lamb, M.P., Fischer, W.W., Ewing, R.C., McElroy, B.J., Williams, R.M., 2019. Formation of sinuous ridges by inversion of river-channel belts in Utah, USA, with implications for Mars. Icarus 332, 92-110. https://doi.org/10.1016/j.icarus.2019.04.019.

Hiller, K.H., 1979. Geologic map of the Amenthes Quadrangle of Mars. U.S. Geological Survey, IMAP 1110, Scale 1:5,000,000. https://doi.org/10.3133/i1110.

Hungr, O., Leroueil, S., Picarelli, L., 2014. The Varnes classification of landslide types, an update. Landslides 11(2), 167-194. https://doi.org/10.1007/s10346-013-0436-y.

Irwin, R.P., Howard, A.D., 2002. Drainage basin evolution in Noachian Terra

Cimmeria, Mars. J. Geophys. Res. Planets 107 (E7). https://doi.org/10.1029/2001JE001818.

Irwin III, R.P., Watters, T.R., Howard, A.D., Zimbelman, J.R., 2004. Sedimentary resurfacing and fretted terrain development along the crustal dichotomy boundary, Aeolis Mensae, Mars. J. Geophys. Res. Planets 109(E9). https://doi.org/10.1029/2004JE002248.

Irwin, R.P., Howard, A.D., Craddock, R.A., Moore, J.M., 2005. An intense terminal epoch of widespread fluvial activity on early Mars: 2. Increased runoff and paleolake development. J. Geophys. Res. Planets 110 (E12). https://doi.org/10.1029/2005JE002460.

Ke, Y., Solomatov, V.S., 2006. Early transient superplumes and the origin of the Martian crustal dichotomy. J. Geophys. Res. Planets 111(E10). https://doi.org/10.1029/2005JE002631.

King, E.A., 1978. Geologic map of the Mare Tyrrhenum Quadrangle of Mars. US Geological Survey Report, IMAP 1073. https://doi.org/10.3133/i1073.

Kneissl, T., van Gasselt, S., Neukum, G., 2011. Map-projection-independent crater size-frequency determination in GIS environments—new software tool for ArcGIS. Planet. Space Sci. 59 (11), 1243–1254. https://doi.org/10.1016/j.pss.2010.03.015.

Levy, J.S., Head, J.W., Marchant, D.R., 2007. Lineated valley fill and lobate debris apron stratigraphy in Nilosyrtis Mensae, Mars: Evidence for phases of glacial modification of the dichotomy boundary. J. Geophys. Res. Planets 112(E8). https://doi.org/10.1029/2006JE002852.

Malin, M.C., Bell, J.F., Cantor, B.A., Caplinger, M.A., Calvin, W.M., Clancy, R.T., Lee, S.W., 2007. Context camera investigation on board the Mars Reconnaissance

Orbiter. J. Geophys. Res. Planets 112 (E5). https://doi.org/10.1029/2006JE002808.

McCauley, J.F., Carr, M.H., Cutts, J.A., Hartmann, W.K., Masursky, H., Milton, D.J., Sharp, R.P., Wilhelms, D.E., 1972. Preliminary Mariner 9 report on the geology of Mars, Icarus 17, 289. https://doi.org/10.1016/0019-1035(72)90003-6.

McEwen, A.S., Eliason, E.M., Bergstrom, J.W., Bridges, N.T., Hansen, C.J., Delamere, W.A., Grant, J.A., Gulick, V.C., Herkenhoff, K.E., Keszthelyi, L., Kirk, R.L., Mellon, M.T., Squyres, S.W., Thomas, N., Weitz, C.M., 2007. Mars reconnaissance orbiter's high resolution imaging science experiment (HiRISE). J. Geophys. Res. Planets 112 (E5). https://doi.org/10.1029/2005JE002605.

McGill, G.E., 2000. Crustal history of north central Arabia Terra, Mars. J. Geophys. Res. Planets 105(E3), 6945-6959. https://doi.org/10.1029/1999JE001175.

McGill, G.E., Dimitriou, A.M., 1990. Origin of the Martian global dichotomy by crustal thinning in the late Noachian or early Hesperian, J. Geophys. Res. 95, 12,595–12,605. https://doi.org/10.1029/JB095iB08p12595.

McGill, G.E., Squyres, S.W., 1991. Origin of the Martian crustal dichotomy: Evaluating hypotheses. Icarus 93(2), 386-393. https://doi.org/10.1016/0019-1035(91)90221-E.

Michael, G.G., 2013. Planetary surface dating from crater size–frequency distribution measurements: multiple resurfacing episodes and differential isochron fitting. Icarus 226 (1), 885–890. https://doi.org/10.1016/j.icarus.2013.07.004.

Michael, G.G., Neukum, G., 2010. Planetary surface dating from crater size–frequency distribution measurements: partial resurfacing events and statistical age uncertainty. Earth Planet. Sci. Lett. 294 (3), 223–229. https://doi.org/10.1016/j.epsl.2009.12.041.

Morgan, F., Seelos, F.P., Murchie, S.L., the CRISM Team, 2014. CRISM analysis toolkit (CAT). In: Gaddis, R.G., Hare, T., Beyer, R. (Eds.), Summary and Abstracts of the Planetary Data Workshop, June 2012: Open-File Report 2014-1056. U.S. Geological Survey, Reston, VA, USA, pp. 125–126.

Morgan, G.A., Head, J.W., Marchant, D.R., 2009. Lineated valley fill (LVF) and lobate debris aprons (LDA) in the Deuteronilus Mensae northern dichotomy boundary region, Mars: constraints on the extent, age and episodicity of Amazonian glacial events. Icarus 202(1), 22–38. https://doi.org/10.1016/j.icarus.2009.02.017.

Murchie, S., et al., 2007. Compact reconnaissance imaging spectrometer for Mars (CRISM) on Mars reconnaissance orbiter (MRO). J. Geophys. Res. Planets 112 (E5). https://doi.org/10.1029/2006JE002682.

Parenti, C., Gutiérrez, F., Baioni, D., García-Arnay, Á., Sevil, J., Luzzi, E., 2020. Closed depressions in Kotido crater, Arabia Terra, Mars. Possible evidence of evaporite dissolution-induced subsidence. Icarus 341, 113680. https://doi.org/10.1016/j.icarus.2020.113680

Poulet, F., Bibring, J.P., Mustard, J.F., Gendrin, A., Mangold, N., Langevin, Y., Arvidson, R.E., Gondet, B., Gomez, C., the Omega Team, 2005. Phyllosilicates on Mars and implications for early Martian climate. Nature 438 (7068), 623–627. https://doi.org/10.1038/nature04274.

Reese, C.C., Orth, C.P., Solomatov, V.S., 2010. Impact origin for the Martian crustal dichotomy: Half emptied or half filled? J. Geophys. Res. Planets 115(E5). https://doi.org/10.1029/2009JE003506.

Reese, C.C., Orth, C.P., Solomatov, V.S., 2011. Impact megadomes and the origin of the martian crustal dichotomy. Icarus 213(2), 433-442. https://doi.org/10.1016/j.icarus.2011.03.028.

Rivera-Hernández, F., Palucis, M.C., 2019. Do deltas along the crustal dichotomy boundary of Mars in the Gale crater region record a northern ocean? Geophys. Res. Lett. 46, 8689–8699. https://doi.org/10.1029/2019GL083046.

Roberts, J.H., 2015. Hemispheric Dichotomy (Mars). In: Hargitai H., Kereszturi Á. (eds) Encyclopedia of Planetary Landforms. Springer, New York, NY. https://doi.org/10.1007/978-1-4614-3134-3_649.

Roberts, J.H., Zhong, S., 2006. Degree- 1 convection in the Martian mantle and the origin of the hemispheric dichotomy. J. Geophys. Res. Planets 111(E6). https://doi.org/10.1029/2005JE002668.

Scott, D.H., Carr, M.H., 1978. Geologic Map of Mars: U.S. Geological Survey Investigations Series, I-1083, Scale 1:25,000,000. http://pubs.er.usgs.gov/publication/i1083.

Seu, R., Phillips, R. J., Biccari, D., Orosei, R., Masdea, A., Picardi, G., Safaeinili, A., Campbell, B.A., Plaut, J.J., Marinangeli, L., Smrekar, S.E., Nunes, D.C., 2007. SHARAD sounding radar on the Mars Reconnaissance Orbiter. J. Geophys. Res. Planets 112(E5). https://doi.org/10.1029/2006JE002745.

Sharp, R.P., Malin, M.C., 1975. Channels on mars. Geol. Soc. Am. Bull. 86(5), 593-609. https://doi.org/10.1130/0016-7606(1975)86%3C593:COM%3E2.0.CO;2.

Skinner Jr, J.A., Tanaka, K.L., 2003. How should planetary map units be defined? Lunar and Planetary Science Conference Abstracts vol. 34 (p. #2100). Retrieved from: https://www.lpi.usra.edu/meetings/lpsc2003/pdf/2100.pdf.

Skinner Jr, J.A., Tanaka, K.L., 2018. Geological Map of the Nepenthes Planum Region, Mars. US Geological Survey Scientific Investigations Map 3389, Scale 1:1,506,000. https://doi.org/10.3133/sim3389.

Sleep, N.H., 1994. Martian plate tectonics. J. Geophys. Res. Planets 99(E3), 5639-5655. https://doi.org/10.1029/94JE00216.

Solomon, S.C., Aharonson, O., Aurnou, J.M., Banerdt, W.B., Carr, M.H., Dombard, A.J., Frey, H.V., Golombek, M.P., Hauck, S.A. II, Head, J.W. III, Jakosky, B.M., Johnson, C.L., McGovern, P.J., Neumann, G.A., Phillips, R.J., Smith, D.E., Zuber, M.T., 2005. New perspectives on ancient Mars. Science 307, 1214–1220, https://doi.org/10.1126/science.1101812.

Strahler, A.N., 1952. Hypsometric (area-altitude) analysis of erosional topography. Geol. Soc. Am. Bull. 63(11), 1117-1142. https://doi.org/10.1130/0016-7606(1952)63[1117:HAAOET]2.0.CO;2.

Summons, R.E., Amend, J.P., Bish, D., Buick, R., Cody, G.D., Des Marais, D.J., Dromart, G., Eigenbrode, J.L., Knoll, A.H., Sumner, D.Y., 2011. Preservation of martian organic and environmental records: final report of the Mars Biosignature Working Group. Astrobiology, 11(2), 157-181. https://doi.org/10.1089/ast.2010.0506.

Tanaka, K.L., Golombek, M.P., Banerdt, W.B., 1991. Reconciliation of stress and structural histories of the Tharsis region of Mars. J. Geophys. Res. Planets 96(E1), 15617-15633. https://doi.org/10.1029/91JE01194.

Tanaka, K.L., Scott, D.H., Greeley, R., 1992a. Global stratigraphy. In: Kieffer HH, Jakosky BM, Snyder CW, Matthews MS (eds) Mars. University Arizona Press, Tucson, pp 345–382.

Tanaka, K.L., Chapman, M.G., Scott, D.H., 1992b. Geologic map of the Elysium region of Mars. US Geological Survey Report, IMAP 2147. https://doi.org/10.3133/i2147.

Tanaka, K.L., Skinner, J.A., Hare, T.M., 2005. Geologic map of the northern plains of Mars. US Geological Survey Scientific Investigations Map 2888, Scale 1:15,000,000. https://doi.org/10.3133/sim2888.

Tanaka, K.L., Skinner Jr., J.A., Dohm, J.M., Irwin III, R.P., Kolb, E.J., Fortezzo, C.M., Platz, T., Michael, G.G., Hare, T.M., 2014. Geologic Map of Mars. US Geological Survey Scientific Investigations Map 3292, Scale 1:20,000,000. pamphlet 43 p. https://doi.org/10.3133/sim3292.

Viviano, C.E., Seelos, F.P., Murchie, S.L., Kahn, E.G., Seelos, K.D., Taylor, H.W., Taylor, K., Ehlmann, B.L., Wiseman, S.M., Mustard, J.F., Morgan, M.F., 2014. Revised CRISM spectral parameters and summary products based on the currently detected mineral diversity on Mars. J. Geophys. Res. Planets 119(6), 1403–1431. https://doi.org/10.1002/2014JE004627.

Viviano-Beck, C.E., et al., 2015.MRO CRISM type spectra library. NASA Planetary Data System. Retrieved from: http://crismtypespectra.rsl.wustl.edu.

Warner, N.H., Gupta, S., Calef, F., Grindrod, P., Boll, N., Goddard, K., 2015. Minimum effective area for high resolution crater counting of Martian terrains. Icarus 245, 198–240. https://doi.org/10.1016/j.icarus.2014.09.024.

Watters, T.R., 1988. Wrinkle ridge assemblages on the terrestrial planets. J. Geophys. Res. Solid Earth 93(B9), 10236-10254. https://doi.org/10.1029/JB093iB09p10236.

Watters, T.R., 1993. Compressional tectonism on Mars. J. Geophys. Res. Planets 98(E9), 17049-17060. https://doi.org/10.1029/93JE01138.

Watters, T.R., 2003a. Lithospheric flexure and the origin of the dichotomy boundary on Mars, Geology 31, 271–274. https://doi.org/10.1130/0091-7613(2003)031%3C0271:LFATOO%3E2.0.CO;2.

Watters, T.R., 2003b. Thrust faults along the dichotomy boundary in the eastern hemisphere of Mars, J. Geophys. Res. Planets 108(E6), 5054. https://doi.org/10.1029/2002JE001934.

Watters, T.R., Robinson, M.S., 1999. Lobate scarps and the Martian crustal dichotomy.

J. Geophys. Res. Planets 104(E8), 18981-18990. https://doi.org/10.1029/1998JE001007.

Watters, T.R., McGovern, P.J., 2006. Lithospheric flexure and the evolution of the dichotomy boundary on Mars. Geophys. Res. Lett. 33(8). https://doi.org/10.1029/2005GL024325.

Watters, T.R., Solomon, S.C., Robinson, M.S., Head, J.W., André, S.L., Hauck II, S.A., Murchie, S.L., 2009. The tectonics of Mercury: The view after MESSENGER's first flyby. Earth Planet. Sc. Lett. 285(3-4), 283-296. https://doi.org/10.1016/j.epsl.2009.01.025.

Wilhelms, D.E., 1990. Geologic mapping. In: Greeley, R., Batson, R.M. (Eds.), Planetary Mapping. Cambridge University Press, NY, pp. 208-260.

Wilhelms, D.E., Squyres, S.W., 1984. The Martian hemispheric dichotomy may be due to a giant impact. Nature 309(5964), 138-140. https://doi.org/10.1038/309138a0.

Zhong, S., Zuber, M.T., 2001. Degree-1 mantle convection and the crustal dichotomy on Mars. Earth Planet. Sc. Lett. 189(1-2), 75-84. https://doi.org/10.1016/S0012-821X(01)00345-4.

Zuber, M.T., Smith, D.E., Solomon, S.C., Muhleman, D.O., Head, J.W., Garvin, J.B., 1992. The Mars Observer laser altimeter investigation. J. Geophys. Res. Planets 97 (E5), 7781–7797. https://doi.org/10.1029/92JE00341.

Zuber, M.T., Solomon, S.C., Phillips, R.J., Smith, D.E., Tyler, G.L., Aharonson, O., Balmino, G., Banerdt, W.B., Head, J.W., Johnson, C.L., Lemoine, F.G., McGovern, P.J., Neumann, G.A., Rowlands, D.D., Zhong, S., 2000. Internal structure and early thermal evolution of Mars from Mars Global Surveyor topography and gravity. Science 287(5459), 1788-1793. https://doi.org/10.1126/science.287.5459.1788.

Declaration of interests

☒The authors declare that they have no known competing financial interests or personal relationships that could have appeared to influence the work reported in this paper.

☐The authors declare the following financial interests/personal relationships which may be considered as potential competing interests:

Highlights:

- Geological-geomorphological framework of NW Terra Cimmeria and SE Nepenthes Mensae
- A rich and long-term geological history spanning from Early Noachian to recent times
- Compressional and extensional stresses occurred from Late Noachian to Late Hesperian
- Extensional tectonics controlled the development and evolution of the dichotomy
- Fluvio-lacustrine activity played a fundamental morphogenetic role on the landscape